Stress minimization for lattice structures. Part I: Micro-structure design

A Ferrer, P Georoy-Donders, G. Allaire

Stress minimization for lattice structures. Part I: Micro-structure design

A. Ferrer*[1], P. Geoffroy-Donders[2], and G. Allaire[1]

[1]CMAP, École Polytechnique, Institut Polytechnique de Paris, 91128 Palaiseau, France.
[2]Arts et Métiers Paristech, 151, Boulevard de l'hôpital, 75013 Paris, France

June 30, 2020

Abstract

Lattice structures are periodic porous bodies which are becoming popular since they are a good compromise between rigidity and weight and can be built by additive manufacturing techniques. Their optimization has recently attracted some attention, based on the homogenization method, mostly for compliance minimization [1], [2], [3]. The goal of the present two-part work is to extend this lattice optimization to an objective function involving stress minimization. As is well known in structural optimization, stress optimization is a very difficult problem. While the second part of our work will be devoted to the macroscopic optimization process itself, the present first part is devoted to the choice of a parametrized periodicity cell that will be optimally selected in the second part of this work. Designing the right periodicity cell is of paramount importance for the success of the optimization process. For manufacturability reasons it is crucial that this cell is parametrized by just a few parameters. According to homogenization theory, one has to compute the effective elasticity tensor, as well as the corrector terms accounting for possible stress concentrations at the cell or microscopic scale. For compliance minimization a standard choice in 2-d is a square cell with a rectangular hole, or a rank-2 laminate. However, since these microstructures feature corners, they are not optimal for stress minimization. Therefore we propose a square cell with a super-ellipsoidal hole which exhibits no corners. This type of cell is parametrized in 2-d by one orientation angle, two semi-axis and an exponent in its defining equation which can be interpreted as a corner smoothing parameter. We first analyse the influence of these parameters on the stress norm by performing some numerical experiments. Second, the optimal corner smoothing parameter is found for each possible micro-structure and macroscopic stress. In order to obtain an optimal micro-structure that depends only on geometrical parameters and not on the stress value, we further average (with specific weights) the optimal smoothing exponent with respect to the macroscopic stress. For simplicity, the optimal values of the corner smoothing parameter are interpolated by an analytical approximated formula. Finally, to validate the results, we compare our optimal super-ellipsoidal hole with the Vigdergauz micro-structure which is known to be optimal for stress minimization in some special cases.

1 Introduction

Limiting the maximum stress value that could appear in a structural domain is a crucial issue in mechanical engineering. Indeed many undesired effects, like damage, plasticity and fracture, may appear if the maximum stress exceeds a certain threshold value. For this reason it is very important that the design of structures takes into account the control of some measure or norm of the stress field. Typically, an optimal design process takes into account some stress constraint or directly minimizes the point-wise maximum stress or some approximating averaged norm. It turns out that this problem is extremely hard to solve.

Many different approaches have been developed to solve it. Based on the SIMP method, the early work [4] proposed a relaxation of the stress constraint for avoiding the singularity problem. However

*alex.ferrer@polytechnique.edu

the stress constraints were considered point-wise which makes the problem intractable as the mesh size increases. To deal with this aspect, in [5], the point-wise constraint was substituted by a finite L^p-norm ($p = 4$ in the examples). A comprehensive review of the topic and a SIMP-based interpolation for dealing with the singularity problem is presented in [6]. More recently, compliant mechanisms were optimized in [7] for stress constraints with a finite L^p-norm ($p = 12$). Typically, in the SIMP approach for stress minimization, two different material interpolations are used: one for the constitutive tensor (usually the elasticity tensor is proportional to ρ^p where ρ is the material density) and another one for the stress evaluation. The first interpolation is known, in some cases, to correspond to real microstructures. However, the second interpolation (for the stress) cannot be interpreted in terms of homogenized stresses for the previous, or any other, micro-structures.

An alternative to the use of SIMP and intermediate densities is the level-set method. This was demonstrated in [8] where a L^p-norm ($p = 10$) of the stress was minimized for 2-d and 3-d examples. Instead of using the classical shape derivative, the authors of [9] proposed a variant of the level-set algorithm based on the notion of topological derivative. In [10], the authors also used a level-set algorithm for multiple load cases and proposed different stress criteria in different regions of the structure.

In any case, these previous works, either with the SIMP or the level-set approach, were focusing on macroscopic structures. They did not consider domains with fine details or, more precisely, in such cases they would require significantly fine meshes. Consequently, for computational cost reasons these methods cannot be applied to the so-called lattice materials which are finely graded structures with a porous microstructure. Lattice materials recently appear as a serious alternative to more classical materials since they can be built thanks to the most advanced additive manufacturing technologies. The goal of the present work is to propose an homogenization method for stress minimization applied to these lattice structures. Homogenization is known to be a convenient theory to describe averaged of effective behaviour of graded structures or composite materials and has been successfully used in topology optimization since many years (see the textbook [11] for a brief history of this method). The homogenization method has already been applied for some stress optimization problems. For example, [12] maximized the torsional rigidity of functional graded composite materials made by a matrix with fibres inclusions, [13] extended the previous theory by additionally solving its corresponding inverse homogenization problem and [14] used composites (rank-n laminates) for minimizing the stress norm. A key point in these contributions is that homogenization theory does not only define averaged or effective properties for the elastic properties but also introduce the concept of corrector terms for approaching the true stress and strain tensors in an heterogeneous medium, beyond the simple homogenized or averaged stress or strain tensor. In particular, it yields the notion of amplification stress factors, or amplificators, which corrects the averaged macroscopic stress in order to have a reliable evaluation of the local microscopic stress concentration. Indeed, it is well known that microscopic heterogeneities may cause stress concentrations. Thus, in contrast with interpolation approaches like the SIMP method, [14] proposed a mechanically sound evaluation of microscopic stress effects. However, the stress norm used was not very large (L^p with $p = 2$) and the final shapes are intrinsically multi-scale (use of rank-n laminates) and thus hard to manufacture. Actually these previous works were concerned with the stress optimization of macroscopic structures, through a penalization approach which eliminates intermediate densities.

On the contrary, the present work is interested in lattice structures which are porous materials with varying macroscopic material densities. Following the pioneer work [3], it fits in the framework of the so-called de-homogenization method, which has recently been applied in [1], [2] for compliance minimization of lattice structures. The main feature of the de-homogenization method is that, after optimizing an homogenized model based on a parametrized and orientable periodicity cell, it reconstructs a globally smooth, graded and curved lattice, which is near optimal. The main novelty of our work is to extend this de-homogenization approach to stress minimization problems, introducing the additional ingredient of stress amplification factors. Let us acknowledge that there are other works on stress constraints in the optimization of lattice structures (see e.g. [15] and [16]). However, they do not consider the orientation of the cells as a design variable and they do not rely on the de-homogenization approach.

Let us describe in some more details the de-homogenization method of [1], [2], [3] which is a very efficient technique for designing lattice structures. This method consists in pre-computing first the homogenized properties of a family of micro-structures parametrized by a few geometrical variables. Then, a standard macroscopic optimization problem is solved in terms of these geometrical variables in combination with the orientation of the micro-structure. Finally, a de-homogenization technique is used for describing the global structure in terms of a porous microscopic geometry with a clear interface and full details. As already mentioned, we extend these previous works to the context of stress minimization. Note that some promising results can already be found in [17]. Our contribution is split in two parts. Part I focuses on the design of an appropriate periodic microstructure which, apart from being nearly optimal for stress minimization, perfectly fits in the framework of [1], [2], [3]. On the other hand, Part II [18] is devoted to the optimization of a macroscopic structure for stress minimization, where at each point the design variables are the geometric parameters and the orientation of an underlying periodic cell (the optimal super-ellipsoidal hole, obtained in the present Part I).

The periodic microstructure proposed in the present work are merely *nearly optimal* for several reasons. First, to define a notion of optimality a proper cost, i.e., a measure of stress, must be defined. There are several possibilities: to take into account the full stress tensor, only its deviatoric part, some scalar criterion like von Mises or Tresca or to consider the maximum value or some L^p norm. Here we choose the maximum value, in the periodic cell, of the Frobenius norm of the full stress. These stresses are computed by solving the so-called cell problem with periodic boundary condition and imposed averaged or homogenized stress. Second, for manufacturability reasons, we seek a simple periodicity cell, parametrized by just a few parameters. Restricting our search to periodic cells excludes other microstructures, like rank-n laminates, which are certainly more optimal but are unfortunately multi-scale and thus hard to manufacture. Our choice is a super-ellipsoidal hole in a square cell. Clearly other choices of the unit cell would have been possible which could lead to more optimal properties, at the expense of more involved parametrizations. In other words, our choice is a compromise between simplicity and optimality. Furthermore, it is well-known that the optimal shape of a hole for this type of problem depends on the applied load, namely on the averaged or homogenized stress. However, for the sake of simplicity, we decide to find a periodic microstructure which is independent of the applied stress. Therefore, we apply an averaging process to find a microstructure which is nearly optimal for a whole family of stresses and not merely for one load. On the same token, to reduce the dependence of the microstructure to the imposed stress, we decide to always orientate the unit cell (or similarly the corresponding orthotropic effective Hooke's tensor) with the principal axis of the imposed stress. This orientation is known to be optimal for compliance minimization by a result of Pedersen [19]. Although it is not obvious that it is also optimal for stress minimization, it makes sense from the mechanical point of view. In any case, eliminating the pure shear component of the applied stress, by orientating accordingly the micro-structure, induces a drastic simplification of the optimization process.

The paper is organized as follows. Section 2 recalls the necessary results of homogenization in order to define, not only the homogenized or effective Hooke's law, but also the corrector terms which, upon suitable averaging, yields the stress amplification factors. Although the theory is valid in any space dimension, from now on we restrict ourselves to 2-d. In Section 3 the super-ellipsoidal hole in a square periodicity cell is precisely defined. Its boundary is parametrized by the two values of its semi-axis m_1, m_2 and an exponent $q \geq 2$ in its governing equation (25) ($q = 2$ corresponds to a standard ellipse while higher values make it more and more like a rectangle). For further use in the optimization process, we replace the semi-axis parameters m_1, m_2 by the volume fraction ρ and a semi-axis ratio ξ which, together with the exponent q, characterize the super-ellipse. There are already some works in shape optimization for stress minimization featuring super-ellipsoidal holes, most notably [20] and [21]. In the former, a level-set representation of the geometry is combined with an XFEM formulation to deal with the sharp interface. Additionally, the optimal micro-structure is solved in terms of the volume fraction and the macroscopic strain. In the latter, the authors used a SIMP-based approach and the goal is to find the optimal semi-axis ratio and corner smoothing parameter to minimize the maximum stress for a micro-structure with a given volume fraction and loaded by a certain macroscopic strain (or stress). Here our goal is different since we want to design an optimal micro-structure which depends only on

the volume fraction and on the geometrical variables and not on the applied macroscopic stress. Note that the symmetry of the proposed super-ellipsoidal hole provides orthotropic homogenized tensors.

In Section 4, some numerical experiments are performed to gain insight on the super-ellipsoidal geometry. In particular, we compare homogenized tensors and stress amplification factors for values of the smoothing exponent q of the super-ellipse (ranging from $q = 2$, ellipses, to $q = +\infty$, rectangles). We also compare, for the same geometry, various stress amplification factors corresponding to different values of the exponent p which characterizes the L^p norm of the stresses. Note that the stress amplification tensors play a key role for minimizing the stress norm as demonstrated in [1] and [17]. Section 5 is our main result where we numerically solve the material design problem of minimizing the maximum stress. This optimal design problem is decomposed in three steps. In a first step, for a given applied macroscopic stress, a given volume fraction ρ and a given semi-axis ratio ξ, the optimal smoothing exponent q is computed for minimizing the maximum local stress by solving the optimization problem (33). Note that, since the macroscopic stress is aligned with the microstructure and its amplitude is irrelevant in linearised elasticity, this stress is parametrized by a single scalar parameter ϕ. The optimal super-ellipse exponent $q^* = q^*(\xi, \rho, \phi)$ thus depends on three quantities (ξ, ρ, ϕ). In a second step, the optimal exponent q^* is averaged with respect to ϕ, the stress parameter. The average is not uniform but weighted with a bias in terms of ξ. It is expected that the macroscopic optimization of Part II will favor holes which are more elongated in the direction of the largest principal stress. Indeed, such an optimal behaviour is precisely quantified for rank-2 laminates in 2-d compliance minimization [11]. Here, for stress minimization we propose a kernel to average $q^*(\xi, \rho, \phi)$ with respect to ϕ with more emphasis on values which are more likely to appear for a given ξ. Finally, in a third step, the resulting average optimal exponent $q_N(\xi, \rho)$ is approximated by a simple analytic formula, obtained by a least-square problem. In other words, this three-step process delivers a family of *nearly optimal* microstructures depending on solely two parameters: their volume fraction ρ and an anisotropy parameter ξ (semi-axis ratio). They do not depend on the applied stress but they have been designed to be quite optimal for macroscopic stresses which are likely to appear in the macroscopic optimization of Part II.

Finally, Section 6 is a discussion of the Vigdergauz micro-structure and a comparison with our optimal super-ellipsoidal hole. The Vigdergauz micro-structure, originally introduced in [22], is known to minimize the maximum stress in 2-d for applied stresses with principal stresses having the same sign, namely those which have a positive determinant. They were shown to be also optimal for compliance minimization in [23], which further elucidates many properties of this geometry. By using a similar parametrization for both type of holes, we are able to optimize the smoothing exponent q of the super-ellipse so that it is as close as possible to the Vigdergauz micro-structure. For various examples we found an excellent agreement between these Vigdergauz and optimized super-ellipse micro-structures. However, the latter ones have a much simpler explicit definition, which is an advantage for numerical simulations. Finally, let us conclude this introduction by recalling that the proposed super-ellipsoidal hole will be used in Part II of our work [18] to optimize a macroscopic lattice structure for stress minimization.

2 Setting of the problem

2.1 Stress minimization for classical shapes.

Let us consider a smooth working domain $D \subset \mathbb{R}^N$ (in practice $N = 2$ or 3) and the reference configuration of an elastic body $\Omega \subset D$. The part of the boundary of the domain where the shape Ω is clamped is denoted by Γ_D, while the part where the surface external force g is applied is denoted by Γ_N. It is assumed that Γ_D and Γ_N are subsets of ∂D and are fixed for any $\Omega \subset D$. The volumetric external force is denoted by f. Then, the associated linear elasticity problem is to find the displacement

$u \in H^1(\Omega;\mathbb{R}^N)$ such that

$$\left\{\begin{array}{rcll} -\operatorname{div}(Ae(u)) & = & f & \text{in } \Omega, \\ u & = & 0 & \text{on } \Gamma_D, \\ Ae(u)\cdot n & = & g & \text{on } \Gamma_N, \\ Ae(u)\cdot n & = & 0 & \text{on } \Gamma = \partial\Omega \setminus (\Gamma_D \cup \Gamma_N), \end{array}\right. \tag{1}$$

where A corresponds to the elasticity constitutive tensor. The strain tensor is defined as usual by the symmetric gradient $e(u) = \nabla^s u = (\nabla u + (\nabla u)^T)/2$. The stress tensor is $\sigma = Ae(u)$. We introduce the stress functional $J(\Omega)$ as

$$J(\Omega) = \int_\Omega |\sigma|^p dx,$$

where the stress is obtained from solving (1) and the exponent is $p \in [2,\infty)$. We use in this work the euclidean norm $|\sigma| = \sqrt{\sigma : \sigma}$, but other norms (i.e. Von Mises) are also possible. Introducing a space $\mathcal{K}$ of admissible shapes (for example smooth open subsets of D, the boundary of which contains Γ_D and Γ_N), the stress minimization problem is defined by

$$\begin{array}{ll} \min\limits_{\Omega\in\mathcal{K}} & \displaystyle\int_\Omega |\sigma|^p dx \\ \text{s. t.} & \displaystyle\int_\Omega dx = V^* \end{array} \tag{2}$$

where V^* stands for a given target shape volume. Note that in general, problem (2) is expected to be ill-posed since domains with the same volume but with structure details of smaller length scale may always decrease the cost function [11]. To circumvent this inconvenient, we may relax problem (2) by incorporating composites shapes and by understanding the notion of convergence in a weaker sense, in the sense of homogenization.

2.2 Homogenization and correctors

Let us briefly recall how problem (2) can be relaxed by homogenization, as already explained in [14]. We start by some classical results of homogenization theory (see [11] for details). To simplify the analysis, the shape optimization problem is approximated by a two-phase optimal design problem. More precisely, the elasticity tensor A in (1) is now denoted by A_1 and the void part $D \setminus \Omega$ is filled with a weak or ersatz material with elasticity tensor $A_0 << A_1$. The characteristic function of the subdomain occupied by phase A_1 is called $\chi(x)$ (it takes the value 1 in the phase A_1 and 0 outside).

H-convergence. Homogenization theory is concerned with sequences of shapes or two-phase mixtures. Let χ_ϵ be a sequence of characteristic functions in $L^\infty(D;\{0,1\})$ and let A_ϵ be its corresponding sequence of constitutive tensors, defined by

$$A^\epsilon = (1-\chi^\epsilon)\,A_0 + \chi^\epsilon A_1, \tag{3}$$

to which we associate the displacements u_ϵ solution of the elasticity problem

$$\left\{\begin{array}{rcll} -\operatorname{div}(A^\epsilon e(u_\epsilon)) & = & f & \text{in } D, \\ u_\epsilon & = & 0 & \text{on } \Gamma_D, \\ A^\epsilon e(u_\epsilon)\cdot n & = & g & \text{on } \Gamma_N, \\ A^\epsilon e(u_\epsilon)\cdot n & = & 0 & \text{on } \Gamma = \partial D \setminus (\Gamma_D \cup \Gamma_N), \end{array}\right. \tag{4}$$

and the corresponding stress tensor $\sigma^\epsilon = A^\epsilon e(u^\epsilon)$. Then, the main result of H-convergence theory (see Theorem 1.2.16 of [11]) states that there exists a sub-sequence, still denoted by ϵ, a limit material density $\rho \in L^\infty(D;[0,1])$ and a limit homogenized tensor $A^* \in L^\infty(D;\mathbb{R}^{N^4})$, such that

$$\begin{array}{rcll} \chi^\epsilon & \to & \rho & \text{weakly* in } L^\infty(D;[0,1]) \\ A^\epsilon & \xrightarrow{\text{H}} & A^* & \text{in the sense of H-convergence,} \end{array} \tag{5}$$

where the H-convergence is defined as the two following convergences

$$\begin{aligned} u^\epsilon &\rightharpoonup u \text{ weakly in } H^1(D;\mathbb{R}^N) \\ \sigma^\epsilon &\rightharpoonup \sigma \text{ weakly in } L^2\left(D;\mathbb{R}^{N^2}\right) \end{aligned}$$

where $\sigma = A^* e(u)$ and u is the displacement solution of the homogenized elasticity problem

$$\left\{\begin{array}{rcll} -\operatorname{div}(A^* e(u)) &=& f & \text{in } D, \\ u &=& 0 & \text{on } \Gamma_D, \\ A^* e(u)\cdot n &=& g & \text{on } \Gamma_N, \\ A^* e(u)\cdot n &=& 0 & \text{on } \Gamma = \partial D \setminus (\Gamma_D \cup \Gamma_N). \end{array}\right. \tag{6}$$

In (5) ρ represents the volume fraction of A_1 and A^* represents the homogenized constitutive tensor, or simply homogenized tensor, of the composite. Because the above results are only weak convergences, it is not possible to prove convergence of the associated sequence of stress objective functions. More precisely, one can only deduce that

$$\liminf_{\epsilon\to 0} \int_D |\sigma^\epsilon|^p \,\mathrm{d}x \geq \int_D |\sigma|^p \mathrm{d}x, \tag{7}$$

where, in most cases, the inequality is strict. To circumvent this limitation and obtain a strong convergence of the stresses, corrector tensors have to be introduced.

Corrector tensor in homogenization. According to Lemma 1.3.38 and Theorem 1.3.39 of [11] there exists a sequence of fourth order tensors W^ϵ, called correctors, with the following properties

$$\begin{aligned} W^\epsilon &\rightharpoonup I_4 \text{ weakly in } L^2\left(D;\mathbb{R}^{N^4}\right), \\ A^\epsilon W^\epsilon &\rightharpoonup A^* \text{ weakly in } L^2\left(D;\mathbb{R}^{N^4}\right), \end{aligned} \tag{8}$$

where I_4 is the fourth order identity tensor, and such that

$$\begin{aligned} e(u^\epsilon) - W^\epsilon e(u) &\to 0 \quad \text{strongly in } L^1\left(D;\mathbb{R}^{N^2}\right), \\ \sigma^\epsilon - A^\epsilon W^\epsilon {A^*}^{-1}\sigma &\to 0 \quad \text{strongly in } L^1\left(D;\mathbb{R}^{N^2}\right). \end{aligned} \tag{9}$$

In other words, corrector tensors allow us to move from weak to strong convergence of the strains and stresses. If the homogenized displacement u is smooth enough, the L^1 strong convergence in (9) can be improved in a L^2 strong convergence. Regarding the convergence of the stress σ_ϵ, following [14], its corrector is called an amplification tensor, defined as

$$P^\epsilon = A^\epsilon W^\epsilon {A^*}^{-1} \tag{10}$$

which satisfies $P^\epsilon \rightharpoonup I_4$ weakly in $L^2\left(D;\mathbb{R}^{N^4}\right)$ and, in view of equation (9), yields $\sigma^\epsilon - P^\epsilon\sigma \to 0$ strongly in $L^1\left(D;\mathbb{R}^{N^2}\right)$.

Unfortunately, to improve (7) and obtain an equality instead of an inequality, a L^p strong convergence is required which cannot be deduced in full generality for any $p > 2$. Therefore, from now on, we shall restrict ourselves to periodic homogenization where the corrector results can be further improved.

2.3 Periodic homogenization and correctors

Since H-convergence theory provides no explicit formulas for computing the correctors and amplification tensors, we restrict ourselves to periodic homogenization. The main interest of the periodic case is the availability of such explicit formulas and a better convergence framework which allows us to improve (7) and define a relaxed or homogenized objective function. The main assumption of the periodic setting is that the sequence of characteristic functions χ^ϵ is defined as a periodic function

$$\chi^\epsilon(x) = \chi\left(\frac{x}{\epsilon}\right), \tag{11}$$

where $\chi(y)$ is a Y-periodic function, with the unit cube $Y = (-0.5, 0.5)^N$ and $\epsilon > 0$ is the (small) period of χ^ϵ. The variable $y = x/\epsilon$ is called fast variable and is defined in the domain Y. In the periodic setting, it is not any longer necessary (for technical reasons) to consider a two-phase mixture and, from now on, we come back to the original setting where the ersatz material is void, $A_0 = 0$, and the material phase is $A_1 = A$. In the unit cell Y, material A occupies the subset Y_0 and $Y \setminus Y_0$ is a hole with boundary Γ_{int}. Thus, the material tensor defined in Y is

$$A(y) = \begin{cases} A & y \in Y_0, \\ 0 & y \in Y \setminus Y_0. \end{cases}$$

Periodic homogenization is simpler than the fully general theory of homogenization because the notion of H-convergence can be made more explicit by using two-scale asymptotic expansions (see e.g. [11] for further details). We now recall the main results of interest for our purpose. In particular, correctors, homogenized and amplification tensors can be computed explicitly by solving the so-called cell problems.

Cell problem. Let $H^1_\#\left(Y_0;\mathbb{R}^N\right)$ be the subspace of all functions $u \in H^1(Y_0;\mathbb{R}^N)$ with periodic boundary conditions. For given indices $1 \leq i,j \leq N$, the cell problem amounts to find $w_{ij} \in H^1_\#\left(Y_0;\mathbb{R}^N\right)$ solution of

$$\begin{cases} -\operatorname{div}\left(A\left(e_{ij} + e\left(w_{ij}\right)\right)\right) = 0 & \text{in } Y_0, \\ A\left(e_{ij} + e\left(w_{ij}\right)\right) \cdot n = 0 & \text{on } \Gamma_{int}, \\ y \mapsto w_{ij}(y) & Y_0 - \text{ periodic }, \end{cases} \tag{12}$$

where the tensor $e_{ij} = \frac{1}{2}\left(e_i \otimes e_j + e_j \otimes e_i\right)$ is one element of the canonical basis of symmetric matrices. The solution w_{ij} is called a corrector function. The cell problem admits the following weak form: find $w_{ij} \in H^1_\#\left(Y_0;\mathbb{R}^N\right)$ such that

$$\forall \phi \in H^1_\#\left(Y_0;\mathbb{R}^N\right) \quad \int_{Y_0} Ae\left(w_{ij}\right) : e(\phi) + \int_{Y_0} Ae_{ij} : e(\phi) = 0 \tag{13}$$

which admits a unique solution up to a rigid body motion. The correctors yields an explicit formula for the homogenized constitutive tensor as follows

$$A^*_{ijkl} = \int_{Y_0} A\left(e_{ij} + e\left(w_{ij}\right)\right) : e_{kl} dy \quad \forall\, i,j,k,l \in \{1,...,N\}, \tag{14}$$

or equivalently, using the weak form (13),

$$A^*_{ijkl} = \int_{Y_0} A\left(e_{ij} + e\left(w_{ij}\right)\right) : \left(e_{kl} + e\left(w_{kl}\right)\right) dy\,.$$

The connection with the previous corrector tensor W^ϵ defined in (8) is as follows

$$W^\epsilon(x) = W\left(\frac{x}{\epsilon}\right) \quad \text{with} \quad W_{ijkl}(y) = \begin{cases} I^4_{ijkl} + e\left(w_{ij}\right)_{kl}(y), & y \in Y_0, \\ 0 & y \in Y \setminus Y_0. \end{cases}$$

Similarly, the previous amplification tensor $P^\epsilon = A^\epsilon W^\epsilon A^{*-1}$, defined by (10), reduces to

$$P^\epsilon(x) = P\left(\frac{x}{\epsilon}\right) \quad \text{with} \quad P(y) = \begin{cases} AW(y)A^{*-1} & y \in Y_0, \\ 0 & y \in Y \setminus Y_0. \end{cases}$$

One advantage of the periodic setting is that the strong convergence in (9) can be improved, at least under the assumption that the homogenized solution u is smooth and that boundary layer effects can be neglected (this is the case for rectangular domains D for which it is known that boundary layers

decay exponentially fast inside the domain [24]). More precisely, under these assumptions, one can prove, for any $p \geq 1$,

$$\sigma^\epsilon - P^\epsilon \sigma \to 0 \text{ strongly in } L^p\left(D; \mathbb{R}^{N^2}\right). \tag{15}$$

This convergence property is crucial to pass to the limit in the objective function and improve (7).

In the sequel, we shall use the (more explicit) notation

$$\sigma^{\text{loc}}(y) = P(y)\sigma \tag{16}$$

for the microscopic stress in the unit periodicity cell Y_0 created by a constant macroscopic stress σ. In numerical practice, given σ, one first define the macroscopic strain tensor $e_\sigma = (A^*)^{-1}\sigma$, then one computes the solution $w_\sigma(y)$ of the cell problem (12) where e_{ij} is replaced by e_σ and finally $\sigma^{\text{loc}}(y) = A(y)e(w_\sigma)(y)$.

Homogenized stress norm minimization. Once all the necessary ingredients of homogenization theory are introduced, one can define the homogenized version of the stress minimization problem. For any given periodic characteristic function $\chi(y)$ (defining the perforated unit cell Y_0), the associated sequence χ^ϵ, defined by (11), satisfies

$$\begin{array}{lll} \chi^\epsilon & \to & \rho = \int_Y \chi(y)\,dy \quad \text{weakly* in } L^\infty(D;[0,1]) \\ A^\epsilon & \xrightarrow{\text{H}} & A^* \qquad\qquad\quad \text{in the sense of H-convergence,} \end{array}$$

where A^* is given by (14). Furthermore, because of (15), one can replace, up to small remainders, σ^ϵ by $P^\epsilon\sigma$, which yields

$$\lim_{\epsilon\to 0}\int_D |\sigma^\epsilon|^p dx = \lim_{\epsilon\to 0}\int_D (P^\epsilon\sigma : P^\epsilon\sigma)^{p/2} dx$$

where the limit can easily be computed since P^ϵ is a periodically oscillating sequence

$$\lim_{\epsilon\to 0}\int_D (P^\epsilon\sigma : P^\epsilon\sigma)^{p/2} dx = \int_D\int_{Y_0} (P(y)\sigma(x) : P(y)\sigma(x))^{p/2}\,dydx.$$

We introduce a notation for this limit

$$\mathcal{P}_p(\sigma) = \int_{Y_0} (P(y)\sigma : P(y)\sigma)^{p/2}\,dy, \tag{17}$$

which, for p an even integer, is an homogeneous polynomial of degree p with respect to the entries of σ. Note that all homogenized quantities, namely A^*, ρ and P depend solely on the Y-periodic characteristic function χ. Therefore, the periodic homogenized stress minimization problem is

$$\begin{array}{ll} \min\limits_{\chi} & \displaystyle\int_D \mathcal{P}_p(\sigma)dx \\ \text{s. t.} & \displaystyle\int_D \rho dx = V^* \end{array} \tag{18}$$

where $\sigma = A^* e(u)$ is the stress associated to the solution u of the homogenized problem (6). Problem (18) is a partial relaxation of the original optimization problem (2) because it does not feature all possible composite materials but only those ones obtained by periodic homogenization. In [14] a different partial relaxation was introduced, relying on so-called sequential laminates. In any case, a full relaxation is not available because the set of all composite materials obtained by a general homogenization process is yet unknown in the elasticity setting.

A crucial remark is to acknowledge the fact that, although periodic homogenization was discussed here only for the case of a purely periodic characteristic function $\chi(y)$, it is perfectly legitimate to consider macroscopically modulated periodic functions, like $\chi(x, y)$. In other words, the cell problems and the homogenized properties may vary from point to point in the working domain D and thus depend on x (this is the strategy followed for example in [1]).

2.4 Stress amplification tensor.

The goal of this subsection is to compute the operator $\mathcal{P}_p$ defined by (17). For simplicity, the exponent p is assumed to be an even integer. The case $p = 2$ is the simplest one, and introducing the fourth order tensor

$$\mathbb{P}^{(2)}(y) = P^T(y)P(y) = A^{*-1}W(y)A(y)A(y)W(y)A^{*-1}, \tag{19}$$

it is easily deduced that

$$\mathcal{P}_2(\sigma) = \left(\int_{Y_0} \mathbb{P}^{(2)}(y)dy\right)\sigma : \sigma. \tag{20}$$

The cases $p > 2$ are much more involved. Indeed, in full generality one expects that

$$\mathcal{P}_p(\sigma) = \mathcal{P}_p^* \cdot \Big(\sigma \otimes \cdots \otimes \sigma\Big), \tag{21}$$

where $\mathcal{P}_p^*$ is a $2p$-order tensor with entries given by averages of p-powers of entries of $\mathbb{P}^{(2)}(y)$. This tensor $\mathcal{P}_p^*$ is called the homogenized stress amplification tensor. It is indeed an amplification factor because, in view of (7), it satisfies

$$\mathcal{P}_p(\sigma) \geq |\sigma|^p.$$

To obtain the components of the tensor $\mathcal{P}_p^*$, the idea is to rewrite the tensor product (21), or (17), as an integral of a sum of products between $\mathbb{P}^{(2)}(y)$ and $\sigma \otimes \sigma$. From now on we restrict ourselves to the 2-d case, although all formulas below can easily be generalized to the 3-d case, at the expense of heavier notations. Using Voigt notations in 2-d, we have

$$P(y)\sigma : P(y)\sigma = \mathbb{P}^{(2)}(y)\sigma : \sigma = \begin{bmatrix}\sigma_{11}\sigma_{22}\sigma_{12}\end{bmatrix} \begin{bmatrix} \mathbb{P}^{(2)}_{1111} & \mathbb{P}^{(2)}_{1122} & \mathbb{P}^{(2)}_{1112} \\ \mathbb{P}^{(2)}_{1122} & \mathbb{P}^{(2)}_{2222} & \mathbb{P}^{(2)}_{1222} \\ \mathbb{P}^{(2)}_{1112} & \mathbb{P}^{(2)}_{1222} & \mathbb{P}^{(2)}_{1212} \end{bmatrix} \begin{bmatrix}\sigma_{11} \\ \sigma_{22} \\ \sigma_{12}\end{bmatrix} \tag{22}$$

where the components of the tensor $\mathbb{P}^{(2)}$ are defined by

$$\begin{array}{rcl}
\mathbb{P}^{(2)}_{1111} & = & P^2_{1111} + P^2_{2211} + P^2_{1211}, \\
\mathbb{P}^{(2)}_{2222} & = & P^2_{1122} + P^2_{1222} + P^2_{2222}, \\
\mathbb{P}^{(2)}_{1212} & = & P^2_{1112} + P^2_{2212} + P^2_{1212}, \\
\mathbb{P}^{(2)}_{1122} & = & P_{1111}P_{1122} + P_{2211}P_{2222} + P_{2212}P_{1222}, \\
\mathbb{P}^{(2)}_{1112} & = & P_{1111}P_{1112} + P_{2211}P_{2212} + P_{1211}P_{1212}, \\
\mathbb{P}^{(2)}_{1222} & = & P_{1122}P_{1112} + P_{2222}P_{2212} + P_{1222}P_{1212}.
\end{array}$$

Finally, (22) can be rearranged as a scalar product between 6-th dimensional vectors

$$P(y)\sigma : P(y)\sigma = \begin{bmatrix}\mathbb{P}^{(2)}_{1111} & \mathbb{P}^{(2)}_{2222} & \mathbb{P}^{(2)}_{1212} & 2\mathbb{P}^{(2)}_{1122} & 2\mathbb{P}^{(2)}_{1112} & 2\mathbb{P}^{(2)}_{1222}\end{bmatrix} \begin{bmatrix} \sigma_{11}\sigma_{11} \\ \sigma_{22}\sigma_{22} \\ \sigma_{12}\sigma_{12} \\ \sigma_{22}\sigma_{12} \\ \sigma_{11}\sigma_{12} \\ \sigma_{11}\sigma_{22} \end{bmatrix} = P^{(2)} \cdot \sigma^{(2)}. \tag{23}$$

Stress norm through multinomials. Recall the multinomial theorem

$$(x_1 + \cdots + x_6)^{p/2} = \sum_{|\alpha|=p/2} \binom{p/2}{\alpha} x^\alpha \quad \text{where} \quad \binom{p/2}{\alpha} = \frac{(p/2)!}{\alpha_1! \cdots \alpha_6!},$$

and $x^\alpha = x_1^{\alpha_1}x_2^{\alpha_2}\cdots x_6^{\alpha_6}$ for $\alpha \in \mathbb{N}^6$ and $x \in \mathbb{R}^6$. Furthermore if $x = yz$ in the sense that $x_i = y_iz_i$, $1 \leq i \leq 6$, we introduce the notation $y^\alpha \cdot z^\alpha = y_1^{\alpha_1}\cdots y_6^{\alpha_6}z_1^{\alpha_1}\cdots z_6^{\alpha_6}$. Using this notation for $y = P^{(2)}$ and $z = \sigma^{(2)}$, the amplification tensor can be written as

$$\mathcal{P}_p(\sigma) = \sum_{|\alpha|=p/2} \binom{p/2}{\alpha} \left(\int_{Y_0} \left(P^{(2)}\right)^\alpha dy\right) \cdot \left(\sigma^{(2)}\right)^\alpha = \mathcal{P}_p^* \cdot \Big(\sigma \otimes \cdots \otimes \sigma\Big), \tag{24}$$

where each entry of $\sigma \otimes \cdots \otimes \sigma$ is homogeneous of degree p. The entries of $\mathcal{P}_p^*$ are deduced from (24). In the simplest case of $p = 2$, the number of entries is $N_p = 6$. However, as the exponent is increased $p = \{4, 8, 16\}$, this number increases exponentially $N_p = \{21, 126, 1287\}$.

3 Super-ellipsoidal holes for stress minimization

Now, the goal is to design a microstructure parametrized with a small number of variables such that its corresponding amplification tensor $\mathcal{P}_p^*$ entries are minimized.

3.1 Description of the geometry

For simplicity, in this work we propose a square cell micro-structure with a super-ellipsoidal hole in order to minimize stress concentrations. On the one hand, this geometry generalized both the square/rectangle and the circle/ellipse geometries and includes intermediate holes that continuously varies form one to the other. By using the super-ellipse geometry, it is possible to conveniently round the corners of the square in order to minimize the maximum stress. On the other hand, for adequate values of the parameters, the super-ellipsoidal hole has some resemblance with the Vigdergauz micro-structure which is proven to be optimal in some cases when minimizing the maximum stress [25] (see Section 6 for more details). Note that some other recent works [20, 21] have also proposed to use super-ellipses in shape optimization.

Super-ellipse geometry description. The micro-structure of a unitary square cell $Y = (-0.5, 0.5)^2$ with a super-ellipsoidal hole may be explicitly described as

$$Y_0 = \left\{ \psi(y) < 0; \quad \forall y \in Y \right\}$$

where ψ is the following level-set function

$$\psi\left(y\right) = \quad \left(\frac{y_1}{m_1/2}\right)^q + \left(\frac{y_2}{m_2/2}\right)^q - 1. \tag{25}$$

The super-ellipse is centred at the origin and its semi-axis are $m_1/2$ and $m_2/2$, while the exponent q can be seen as a smoothing corner parameter. From now on, q is called the smoothing exponent, restricted to the values $q \geq 2$.

Super-ellipse volume fraction. Another well-known advantage of a square micro-structure with a super-ellipsoidal hole is that the volume fraction can be explicitly computed by

$$\rho = \int_{Y_0} dy = 1 - c(q) m_1 m_2 \quad \text{with} \quad c(q) = \frac{\Gamma\left(1 + \frac{1}{q}\right)^2}{\Gamma\left(1 + \frac{2}{q}\right)} \tag{26}$$

where Γ is the gamma function.

Super-ellipsoidal hole examples in a unitary square cell. A wide range of shapes can be obtained by just changing the parameters of the super-ellipsoidal hole. Examples of particular interest range from small circles or ellipses, which are well known to be optimal for small holes [25]), to rectangular holes with one of the semi-axis attaining its maximum value (rank-1 laminate case). These and other examples of the family of micro-structures we are considering in this work are shown in Figure 1.

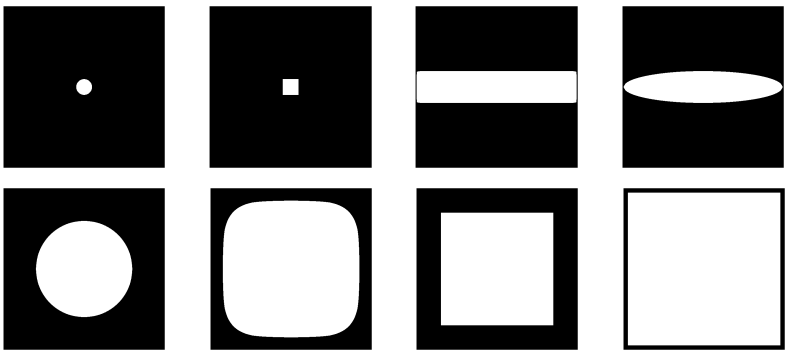

Figure 1: Examples of different super-ellipsoidal holes. From left to right, first line: (i) $m_1 = m_2 = 0.1$; $q = 2$; (ii) $m_1 = m_2 = 0.1$; $q = 32$; (iii) $m_1 = 0.99$; $m_2 = 0.2$; $q = 32$; (iv) $m_1 = 0.99$; $m_2 = 0.2$; $q = 2$. Second line: (i) $m_1 = m_2 = 0.6$; $q = 2$; (ii) $m_1 = m_2 = 0.85$; $q = 4$; (iii) $m_1 = m_2 = 0.7$; $q = 32$; (iv) $m_1 = m_2 = 0.99$; $q = 32$.

Limit cases. Special attention must be paid to the limit cases of super-ellipsoidal holes. Certainly, the micro-structure rigidity becomes singular when the super-ellipsoidal hole touches the square cell boundary, more specifically when $m_i \to 1$ for $i = 1$ or 2. Since we are interested in optimal micro-structure, there is no restriction in introducing bounds on the geometrical parameters, $m_{L_i} \leq m_i \leq m_{U_i}$. From now on, we take in all the examples $m_{L_i} = 0$ and $m_{U_i} = 0.99$. This upper bound will ensure the invertibility of the stiffness matrix in the corresponding macroscopic problem [18]. Furthermore, with such a bound the perforated cells are always properly meshed (in this work we used the library MMG [26]).

Super-ellipse parametrization. To minimize the number of cell parameters, we decide to choose the "best" smoothing exponent q for every value of the parameters m_1 and m_2. This optimal value of q is given by an optimization process described below. Special care is required because this optimization has a tendency to minimize the volume and not to properly round the corners of the super-ellipse. Thus, a volume fraction constraint has to be enforced when solving the optimization problem. See section 5.1 for more details. Then, we replace variables (m_1, m_2) by the semi-axis ratio ξ and the volume fraction ρ. Those variables are defined by

$$\xi = \arctan\left(m_1/m_2\right) \quad \text{and} \quad \rho = 1 - c(q) m_1 m_2. \tag{27}$$

Using the *arctan* function allows us to bound the domain of the semi-axis parameter ξ. Alternatively, the converse relations are:

$$m_1 = \sqrt{\frac{1-\rho}{c(q)\tan(\xi)}} \quad \text{and} \quad m_2 = \sqrt{\frac{(1-\rho)\tan(\xi)}{c(q)}}. \tag{28}$$

Additionally, note that the upper bound on m_i implies the following non-linear bounds

$$\xi_{\min}(\rho, q) = \xi_2(m_{U_2}, q, \rho) \leq \xi \leq \xi_1(m_{U_1}, q, \rho) = \xi_{\max}(\rho, q)$$

where the functions ξ_1 and ξ_2 are defined as

$$\xi_1(m_1, q, \rho) = \arctan\left(\frac{m_1 c(q)}{1-\rho}\right) \quad \text{and} \quad \xi_2(m_2, q, \rho) = \arctan\left(\frac{1-\rho}{m_2 c(q)}\right). \tag{29}$$

Thus, for a given smoothing exponent q, the ranges of the semi-axis and volume fraction are $\xi \in [\xi_{\min}(\rho, q), \xi_{\max}(\rho, q)]$ and $\rho \in [\rho_{\min}(q), 1]$ where $\rho_{\min}(q) = 1 - c(q) m_{U_1} m_{U_2}$. We will call this set the admissible space:

$$\mathcal{V}_{ad}(q) = \Big\{(\xi, \rho) |\ \xi \in [\xi_{\min}(\rho, q), \xi_{\max}(\rho, q)] \quad \text{and} \quad \rho \in [\rho_{\min}(q), 1]\Big\}. \tag{30}$$

Note that the admissible space $\mathcal{V}_{ad}(q=2)$ for an elliptic hole cannot achieve a complete void in the unit cell structure since the minimal volume fraction is about $\rho_{\min}(q=2) \sim 0.2$. Instead, the admissible space $\mathcal{V}_{ad}(q=32)$ for the rectangular hole achieves $\rho_{\min}(q=32) \sim 0.02$. This has a strong impact on most of the topology optimization problems since usually one of the objectives is to reduce the volume of the structure. Note that the largest admissible space is precisely the one for the rectangular and from now on will be called $\mathcal{V}_{ad}^R = \mathcal{V}_{ad}(q=32)$. Thus, rectangular holes may provide the most elongated holes and the lowest volume fraction micro-structures. In Figure 2 are precisely plotted the admissible space for a rectangular hole $\mathcal{V}_{ad}^R = \mathcal{V}_{ad}(q=32)$ and for an elliptic hole $\mathcal{V}_{ad}(q=32)$.

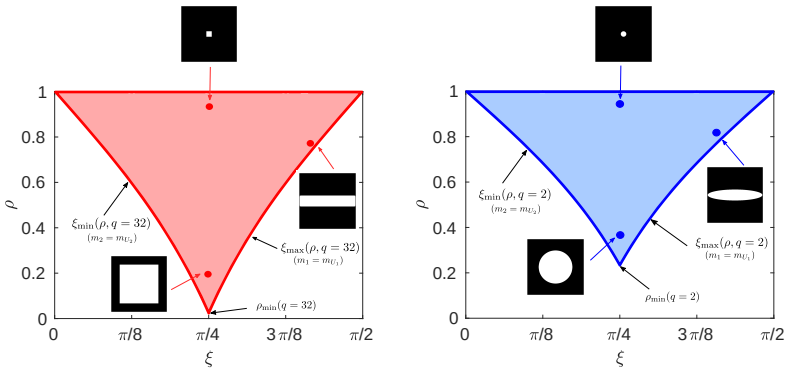

Figure 2: Admissible design space $\mathcal{V}_{ad}(q)$. Clearly, the rectangular case $\mathcal{V}_{ad}(q=32)$ (left image) is larger than the ellipsoidal case $\mathcal{V}_{ad}(q=2)$ (right image). Note that the bounds $\xi_{\min}(\rho, q=32)$ and $\xi_{\max}(\rho, q=32)$ are below $\xi_{\min}(\rho, q=2)$ and $\xi_{\max}(\rho, q=2)$ and that $\rho_{\min}(q=32) < \rho_{\min}(q=2)$.

Note that in this parametrization no orientation of the hole is considered. This is because, according to the optimization strategy of [1], the orientation of the entire square cell will be optimized in the macroscopic topology optimization problem. More details will be given in Part II [18].

3.2 Mesh-size dependency

Certainly, mesh-size effects may appear when minimizing any measure of the stress. It is well-known that the stresses values may tend to infinity at some points (for example, corners) as the mesh-size tends to zero. Since the super-ellipsoidal hole looks like a rectangular hole when the smoothing exponent q goes to infinity, there may be very large point-wise values of the stress in such a case. In Figure 3 we plot the microscopic stress $\sigma_{11}^{\text{loc}}(y)$, defined by (16), for a uniaxial horizontal stress tensor $\sigma_{11} = 1$, $\sigma_{22} = 0$ and $\sigma_{12} = 0$. Indeed for a rectangular hole, the maximum stress diverges when refining the mesh, as expected. On the contrary, for a rounded corner (corresponding to $q = 4$), the maximum stress remains bounded under mesh refinement. For simplicity, in this work, we use a high quality conformal mesh (provided by MMG [26]) to properly describe the perforated cell. We found that it was accurate for evaluating the maximum stress. Other different numerical techniques like filtering [21] or the use of XFEM formulation [20] are also possible. All our numerical results are obtained with a similar mesh size, fine enough to capture the round corners. In this section, as well as in the entire paper, we consider an isotropic elasticity tensor $A = 2\mu I_4 + (\kappa - \mu) I_2 \otimes I_2$ where I_4 and I_2 correspond to the fourth and second order identity tensors. The shear and bulk modulus in 2D are defined by $\mu = \frac{E}{2(1+\nu)}$ and $\kappa = \frac{E}{2(1-\nu)}$ and the values of the Young modulus and Poisson ratio are taken as $E = 1$ and $\nu = 1/3$.

4 Numerical Experiments

In order to get some insight and understand the nature of the problem, we conduct in this section two different numerical experiments. In the first experiment, we study the stiffness and stress norm when considering rectangular or ellipsoidal holes. In the second experiment, we move towards larger stress exponents $p \geq 2$, but this time for different intermediate super-ellipsoidal holes. For simplicity, we

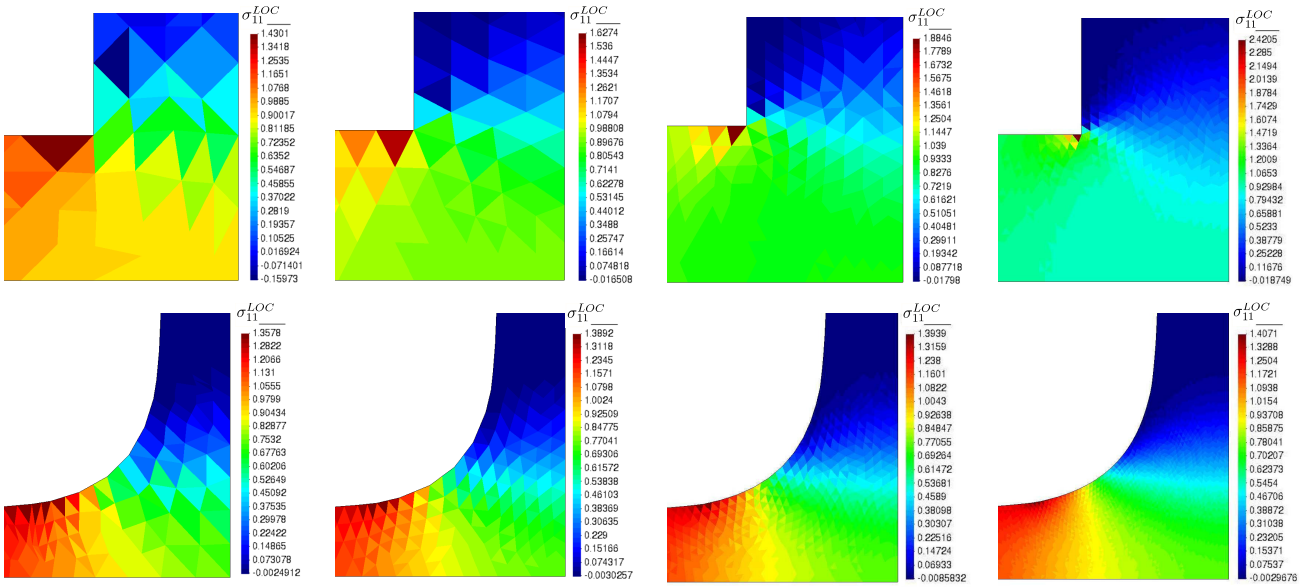

Figure 3: Mesh convergence of the microscopic stress $\sigma_{11}^{\text{loc}}(y)$ when applying a macroscopic stress load $\sigma_{11} = 1$, $\sigma_{22} = 0$ and $\sigma_{12} = 0$ to a square micro-structure with a rectangular and a super-ellipsoidal hole ($q = 4$). The mesh sizes are $h \in \{0.1, 0.05, 0.0025, 0.00125\}$.

only show here a brief summary of the numerical experiments. A detailed and more exhaustive study is reported in the supplementary material of this work [27].

4.1 First numerical experiment: $p = 2$ for rectangular and ellipsoidal holes

In work [1], the optimal lattice structures are obtained by considering rectangular holes when minimizing compliance. Since in this work we focus on stress minimization, we analyse in this first experiment the two simplest cases: rectangular and ellipsoidal holes. Note that the convenience of using rectangular or ellipsoidal holes for compliance minimization is observed through its corresponding homogenized tensor. For the stress norm case, through its corresponding amplification tensor. Thus, in the following, we compare both tensors.

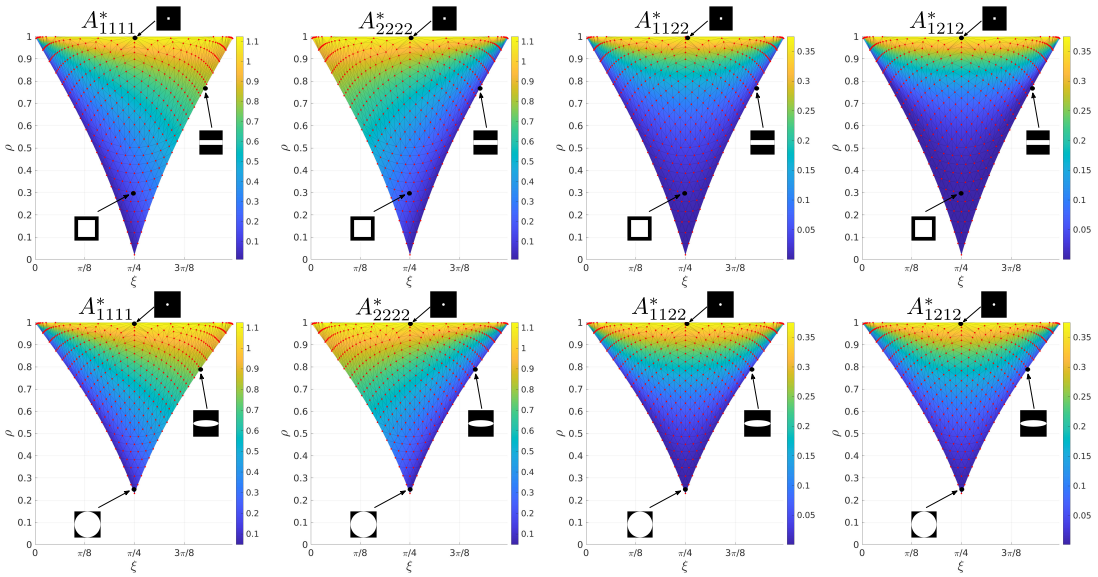

Figure 4: Entries of the homogenized tensor A^* for all possible rectangular and ellipsoidal holes.

Homogenized tensor. In Figure 4, we show all the homogenized tensor entries for both the rectangular and ellipsoidal holes in the admissible design space $\mathcal{V}_{ad}(q)$. Note that comparing in the space

(ξ, ρ) rather than in the space (m_1, m_2) allow us to compare holes with the same volume fraction. For a full comparison in the space (m_1, m_2), see the first experiment in the supplementary material [27]. We first observe in Figure 4 that that both entries A_{1122} and A_{1212} monotonically increases with to the volume fraction ρ. For a given volume fraction ρ, the larger values of A_{1122} and A_{1212} are obtained at symmetric holes ($\xi = \pi/4$). Alternatively, the entries A_{1111} and A_{2222} clearly increases with the design variables m_1 and m_2 rather than with the volume fraction ρ (see the supplementary material [27]). We also see that for a fix volume fraction ρ, the more horizontally elongated the hole, this is $\xi \to \xi_{UB}$ (rank-1 laminate), the larger the component A_{1111}. Similar for A_{2222} with vertical holes. For an explicit difference of the homogenized and amplificator components in the (ρ, ξ) plane and for full numerical details, see the first experiment in the supplementary material [27].

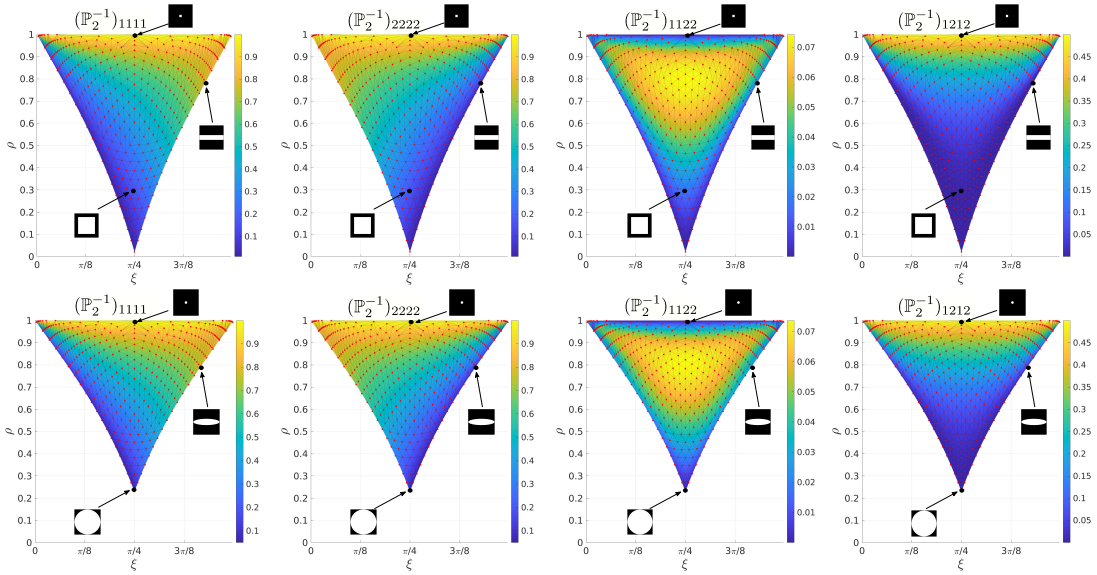

Figure 5: Inverse of amplification tensor $\mathbb{P}_2$ for all possible rectangular and ellipsoidal holes.

Amplification tensor. The influence of considering rectangular or ellipsoidal holes on the stress norm may be easily identified through the amplificator entries. Since small values of the volume fraction may blow up to infinity some amplificator entries, we plot, for clarity proposes, in Figure 5 the inverse of the amplificator tensor $\mathbb{P}_2^{-1}$ in the admissible design space $\mathcal{V}_{ad}(q = 2)$ and $\mathcal{V}_{ad}(q = 32)$. Note that since $\mathbb{P}_2 \geq \mathbb{I}$ in the sense of fourth order tensor, its inverse is bounded from above. In Figure 5, we observe that the component $(\mathbb{P}_2^{-1})_{1122}$ has a concave dependency with ρ and has a maximum value around $\rho \sim 0.8$. The component $(\mathbb{P}_2^{-1})_{1212}$ increases monotonically with ρ and depends weakly on ξ. Symmetric holes have larger $(\mathbb{P}_2^{-1})_{1212}$. Alternatively, as reported in the supplementary material [27], the $(\mathbb{P}_2^{-1})_{1111}$ and $(\mathbb{P}_2^{-1})_{2222}$ depends mainly on the m_1 and m_2 variables directly. For a given volume fraction ρ, we also see that the larger values of $(\mathbb{P}_2^{-1})_{1111}$ is when considering horizontal elongated holes (rank-1). We also observe that the variation of the amplificator entries with (ξ, ρ) variables for rectangular and ellipsoidal holes are similar. However their values are considerably different. A quantitatively and exhaustive comparison of all the amplificator components is reported in the first experiment of the supplementary material [27]. In general, we observe that for small holes ellipsoidal and rectangular holes behave similar and for large holes rectangular holes are preferred, specially for elongated ones ($m_1 \to 1$ or $m_2 \to 1$).

4.2 Second numerical experiment: $p \geq 2$

In this second numerical experiment, we move to general super-ellipses but now considering stress norm exponents $p \geq 2$.

Maximum stress norm. First, we study the maximum stress norm for symmetric ($m_1 = m_2$) representative super-ellipses for two different volume fraction. The idea is to observe the influence of

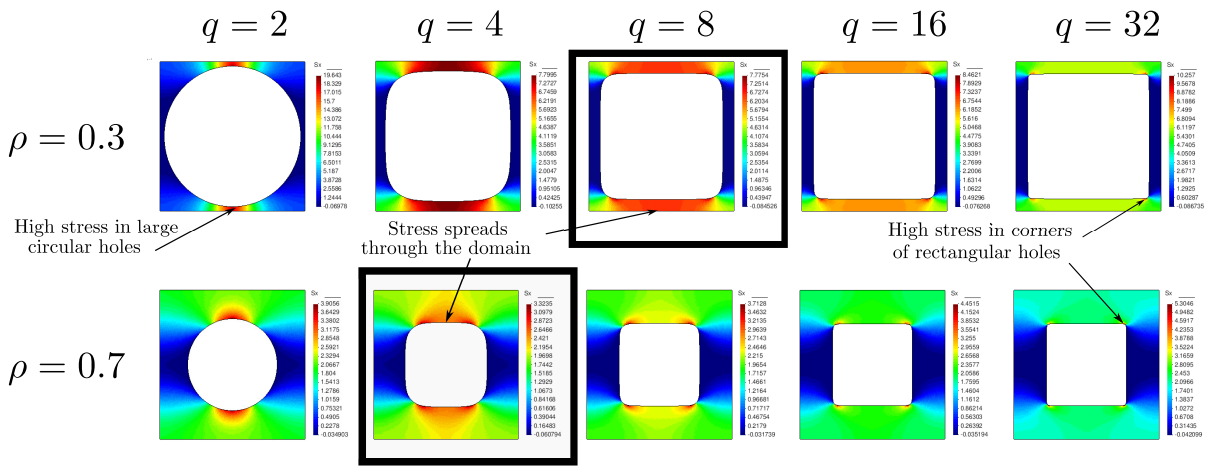

Figure 6: Plot of the local stress field $\sigma_{11}^{\text{loc}}(y)$ for an uni-axial horizontal macroscopic stress tensor $\sigma = [1\ 0\ 0]$. In each row, the case with lowest maximum value of the stress is inscribed in a black box. Rectangular holes with smoothed corners are preferred for large holes. More rounded (ellipsoidal) holes are preferred for intermediate holes.

the smoothing exponent parameter q in the maximum stress norm. In Figure 6, we show the $\sigma_{11}^{\text{loc}}(y)$ component when the cell is loaded with a macroscopic stress $\sigma = [1\ 0\ 0]$. We observe that circles ($q = 2$) and rectangles ($q = 32$) are far from optimal. Circular holes suffers from imposing areas with very small thickness which entails large stress concentrations. Alternatively, squares suffers from imposing infinite curvature in the corners which entails also large stress values. Super-ellipsoidal holes have usually smaller maximum stress when considering intermediate smoothing exponent q values. For example, for $\rho = 0.3$, the optimal exponent is around $q = 8$ and for $\rho = 0.7$ is $q = 4$. In Figure 6, the optimal values are inscribed in a black box. Roughly speaking, optimal exponents evidenced that large stresses are more spatially distributed (larger red areas in Figure 6). See the second experiment of the supplementary material [27] for a more exhaustive study with smaller volume fraction ρ and different macroscopic stress. This representative example evidenced the importance of selecting an optimal smoothing parameter q for minimizing the maximum stress norm.

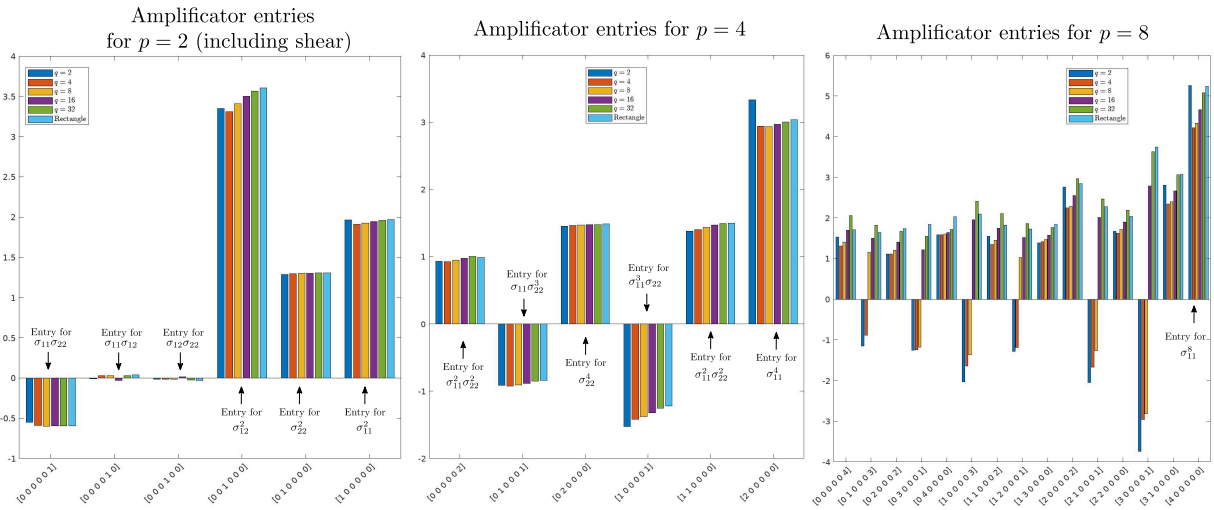

Figure 7: Entries of the stress amplification tensor $\mathcal{P}_p$ for intermediate elongated super-ellipsoidal holes with $2m_1 = m_2$ and $\rho = 0.7$. While the case $p = 2$ includes the shear components, the three other figures do not consider shear terms. For example, the case [1 1 0 0 0 2] represents the amplificator entry that corresponds to $(\sigma_{11}\sigma_{11})^1(\sigma_{22}\sigma_{22})^1(\sigma_{12}\sigma_{12})^0(\sigma_{22}\sigma_{12})^0(\sigma_{11}\sigma_{12})^0(\sigma_{11}\sigma_{22})^2 = \sigma_{11}^4\sigma_{22}^4$.

Amplification tensor entries. Now we study the influence of using different super-ellipsoidal holes on the stress norm with an increasing sequence of stress norm exponent p. More specifically, we analyse the values of the amplificator entries for $p = 2$, $p = 4$ and $p = 8$. In the left image of Figure 7, we plot all the amplificator entries with $p = 2$. We observe that the shear components are the largest ones. This is not a surprise and we recall that in Part II [18], following work [1], we align the micro-structure with the principal stresses and consequently shear entries become irrelevant. Thus, for simplicity, in the middle and left images of Figure 7, we plot no shear components. In Figure 7, we observe an exponential increase of the number of amplificator entries when increasing the stress norm exponent p. We also see that, after shear effects, the larger entries (for this elongated super-ellipsoidal hole) come from pure traction cases. We recall that the amplificator entries are identified through the monomial terms. For example the case [1 1 0 0 0 2] in the horizontal axis of the right image in Figure 7 represents the amplificator entry that corresponds to $(\sigma_{11}\sigma_{11})^1(\sigma_{22}\sigma_{22})^1(\sigma_{12}\sigma_{12})^0(\sigma_{22}\sigma_{12})^0(\sigma_{11}\sigma_{12})^0(\sigma_{11}\sigma_{22})^2 = \sigma_{11}^4\sigma_{22}^4$. A more exhaustive study is also reported in the second experiment of the the supplementary material [27]. We clearly observe that intermediate smoothing exponent q entails smaller values of the amplificator entries. Specially, as we increase the stress norm exponent p. This means again that rectangular and ellipsoidal holes are not optimal and confirms the need of optimizing the smoothing exponent q for minimizing the stress norm.

4.3 Outcome from numerical experiments

After these two numerical experiments, the following conclusions are in order.

(i) For large size holes: rectangles (with rounded corners) are preferred (see Figure 6).

(ii) For medium size and elongated ($\xi \to \xi_{UB}$ or $\xi \to \xi_{LB}$) holes, rectangles (with rounded corners) are also preferred (see supplementary material [27]).

(iii) For medium size symmetric holes ($\xi \sim \pi/4$), circular and super-ellipsoidal holes with small smoothing exponent q behaves better than rectangular holes (see Figure 6).

(iv) For small holes, rectanglular and ellipsoidal holes behave similar (see Figure 7 and supplementary material [27]).

(v) The optimal smoothing exponent depends clearly on the applied macroscopic stress.

(vi) The numerical results also suggest that, in most of the situations, intermediate values of q are better than 2 or 32, i.e. pure ellipsoidal or rectangular holes.

All these outcomes are a guide for the following optimization of the exponent q of the super-ellipsoidal hole.

5 Optimal micro-structure for stress minimization

5.1 Optimization problem

The results of Section 4 outlined that the optimal smoothing exponent q for minimizing the maximum stress depends on many parameters. Let us now systematize the insight obtained from these numerical experiments by solving the following optimization problem: given a semi-axis ratio and a volume fraction $(\xi, \rho) \in \mathcal{V}_{ad}^R$ and a given loading macroscopic stress σ, find the optimal smoothing exponent and the semi-axis parameters $(q^*, m_1, m_2) \in \mathcal{U}_{ad}$ which minimize

$$\min_{(m_1,m_2,q)\in\mathcal{U}_{ad}} \quad \max_{y\in Y_0} \left\{ |\sigma^{\text{loc}}(y)|^2 = P(y)\sigma : P(y)\sigma \right\} \tag{31}$$

where $\sigma^{\text{loc}}(y)$, which depends on (σ, m_1, m_2, q), is the microscopic stress defined by (16) for a constant macroscopic stress σ (its precise computation is explained in section 2.3). The space of admissible smoothing exponent q and semi-axis parameters m_i is defined as

$$\mathcal{U}_{ad} = \left\{ q \in \mathcal{Q}, m_1 \in \mathcal{M}_1, m_2 \in \mathcal{M}_2, \ \arctan(\frac{m_1}{m_2}) = \xi \quad \text{and} \quad 1 - c(q)m_1m_2 = \rho, \ \forall (\xi, \rho) \in \mathcal{V}_{ad}^R \right\}$$

where $\mathcal{Q} = [q_{min}, q_{max}]$ and $\mathcal{M}_i = [m_{L_i}, m_{U_i}]$. We recall that the dependency of the cost with respect to the design variables comes from the definition of the cell Y_0 as

$$Y_0 = \{y \in Y; \quad \psi(y, m_1, m_2, q) < 0\} \tag{32}$$

where $\psi(y, m_1, m_2, q)$ is the level-set that defines the super-ellipsoidal hole (see Section 3.1). Although problem (31) features three independent variables, its two constraints on ρ and ξ allow us to compute explicitly m_1 and m_2, for a given q. Therefore, in the end (31) becomes the following one variable minimization problem

$$\min_{q \in \mathcal{Q}_m} \max_{y \in Y_0} \left\{ |\sigma^{\text{loc}}(y)|^2 = P(y)\sigma : P(y)\sigma \right\} \tag{33}$$

where the admissible space is defined as $\mathcal{Q}_m = [q_{LB}, q_{UB}]$. The values q_{LB},q_{UB} are obtained taking into account that $m_i \in \mathcal{M}_i$ (bounds posed on m_i) by solving

$$\begin{aligned} c(q_{LB}) - \max\left(\frac{(1-\rho)}{m_{L_1}\tan(\xi)}, \frac{(1-\rho)\tan(\xi)}{m_{L_2}}, c(q_{\min})\right) &= 0, \\ c(q_{UB}) - \min\left(\frac{(1-\rho)}{m_{U_1}\tan(\xi)}, \frac{(1-\rho)\tan(\xi)}{m_{U_2}}, c(q_{\max})\right) &= 0, \end{aligned} \tag{34}$$

for all $(\xi, \rho) \in \mathcal{V}_{ad}^R$ where $c(q)$ is the function defined in (26) for computing the volume fraction. Since $c(q)$ is an increasing monotone function, we obtain the values of the bounds q_{LB} and q_{UB} by solving equation (34) with a simple bisection method. Concerning the stress σ in (33), we recall that in this approach, the micro-structure is aligned according to the principal stress, avoiding shear effects. Therefore, in the optimization of the super-ellipsoidal exponent q, we do not consider shear stress, namely we assume $\sigma_{12} = 0$. Additionally, note that the macroscopic stress norm plays no role and consequently σ might be parametrized (in Voigt notation) just by the stress angle ϕ as

$$\sigma = [\sigma_{11} = \sin(\phi) \quad \sigma_{22} = \cos(\phi) \quad \sigma_{12} = 0]. \tag{35}$$

Solving the optimization problem (33) will provide the optimal smoothing exponent $q^*(\xi, \rho, \phi)$. Since the objective function in (33) is a maximum value and thus is non-differentiable, we solve the optimization problem (33) with the standard successive parabolic interpolation algorithm combined with a golden section search [28]. In full generality the stress angle ϕ is defined in $[0, 2\pi]$ (with implicit periodicity condition), but changing ϕ in $\phi + \pi$ simply amounts to change the sign of σ, which leaves invariant the objective function in (31) and (33). Therefore, the stress angle is limited to the $[0, \pi]$ interval and

$$q^*(\xi, \rho, \phi) = q^*(\xi, \rho, \varphi(\phi))$$

where φ is defined as

$$\varphi(\phi) = \begin{cases} \phi & 0 \le \phi \le \pi \\ \phi - \pi & \pi \le \phi \le 2\pi. \end{cases} \tag{36}$$

Thus, in practice, instead of $q^*(\xi, \rho, \phi)$, we directly compute $q^*(\xi, \rho, \varphi)$. To do so, we solve problem (33) by sampling the admissible space V_{ad}^R with 400 points. Instead of uniformly sample the V_{ad}^R, we discretise uniformly $m_1 \in [m_{L_1}, m_{U_1}]$ and $m_2 \in [m_{L_2}, m_{U_2}]$ with 20 points and we use equations 27 (with $q = 32$) to obtain the 400 (ξ, ρ) sample points. The following bounds are set: $m_{L_1} = m_{L_2} = 0.01$, $m_{U_1} = m_{U_2} = 0.99$, $q_{\min} = 2$ and $q_{\max} = 32$. The cell Y_0 is discretised with an unstructured triangular mesh of typical size $h = 0.01$. As an example, Figure 8a displays the convergence of the cost in (33) for $\xi = \pi/4$ ($m_1 = m_2$), $\rho = 0.15$ and $\phi = \pi/4$ ($\sigma_{11} = \sigma_{22}$) and the optimal super-ellipsoidal hole. Our experience is that in all cases, the algorithm converges in roughly $20 \sim 30$ iterations.

Remark that exchanging ϕ with $\pi/2 - \phi$ amounts to rotate the stress tensor by $\pi/2$ (or exchanging the roles of σ_{11} and σ_{22}). Since the super-ellipsoidal hole has cubic symmetry, rotating it by $\pi/2$ is equivalent to exchanging the roles of the semi-axis values m_1 and m_2, namely exchanging ξ with $\pi/2 - \xi$. Therefore, we deduce $q^*(\xi, \rho, \phi) = q^*(\pi/2 - \xi, \rho, \pi/2 - \phi)$, which halves the amount of computations to obtain the optimal exponent q^*. In total, we optimized (in parallel) 400 types of microstructures for 40 load stress angle ϕ values (uniformly distributed). In total, we solved 16000 cases and each optimization problem has taken around 100s of computations.

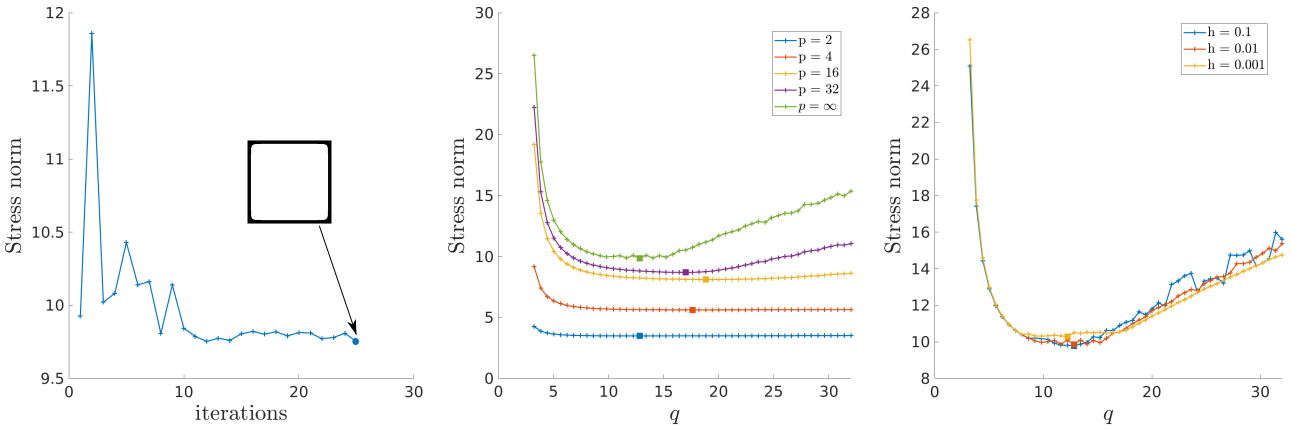

(a) Convergence history of the max stress norm ($p = \infty$)

(b) Variation of $J_p(q)$ for several norm exponents p

(c) Convergence under mesh refinement ($h \to 0$) for the max stress norm ($p = \infty$)

Figure 8: Optimization of the stress norm $J_p(q)$ for $\xi = \pi/4$ ($m_1 = m_2$), $\rho = 0.15$ and $\phi = \pi/4$ ($\sigma_{11} = \sigma_{22}$). In (b) the optimal super-ellipsoid exponent q^* is indicated with a square dot.

Variation of the optimal super-ellipsoidal exponent q with the norm exponent p. Although in problem (33) we considered the $p = \infty$ norm, other choices of p are also possible. For a general $p \geq 2$, the stress norm is defined as

$$J_p(q) = \left(\int_{Y_0} |\sigma^{\text{loc}}(y)|^p \right)^{1/p}. \tag{37}$$

The variation of the stress norm with the optimal smoothing exponent q for different values of p is precisely represented in Figure 8b. The square markers shown in Figure 8b point the minimum value of the stress norm $J_p(q)$. We observe that in this case, for all norm exponent p the optimal holes are neither an ellipsoidal nor a rectangular hole but a super-ellipsoidal hole with an exponent q in the range $(12; 18)$. Additionally, the optimal value q^* of the super-ellipsoidal exponent does not vary monotonically with the norm exponent p. Note also that for small values of p, $J_p(q)$ is almost flat. Thus, the optimal q value is not very relevant since any other value of q will give similar values of $J_p(q)$ Most importantly, the stress norm $J_p(q)$ has larger variations with respect to q for higher values of the norm exponent p. Thus, for large values of p, which is in general the case of interest, the optimization process with respect to q becomes crucial. This example shows that considering $p = \infty$ for designing the optimal super-ellipsoidal hole is an appropriate choice. Note that for large norm exponent p, some oscillations appear in the graph of $J_p(q)$: they are due to numerical discretization errors as explained in the next paragraph.

Convergence under mesh refinement of the optimal super-ellipsoidal exponent. Another aspect to consider when minimizing the stress norm is the mesh size h, specially for large values of p. In Figure 8c the maximum stress norm $J_\infty(q)$ is plotted for different mesh sizes. As expected, the value of $J_\infty(q)$ strongly depends on h for large values of q but is well computed for smaller values, say $q \leq 20$. However, it turns out that in this situation the optimal exponent q^* does not depend much on the mesh size h. Even better, the function $J_\infty(q)$ is rather flat around its minimal value which implies that a small error in the choice of the optimal smoothing exponent q^* entails merely a small change in the max stress norm. However, in other situations where the $J_\infty(q)$ is flat almost everywhere, the mesh discretization plays, as we will see, an important role on choosing the optimal q^*. Prompted by these observations, in all our computations, we use $h = 0.01$.

5.2 Averaging with respect to stress values

The optimal exponent $q^*(\xi, \rho, \sigma)$ clearly depends not only on the geometrical parameters (ξ, ρ) but also on the applied macroscopic stress σ. Recall that σ is parametrized by a stress angle ϕ in (35). In this work, one of the goals is precisely to obtain a parametrized optimal geometry independent of the applied stress. This requirement is made for simplicity or for manufacturing reasons, as explained in [1] or [2]. The idea of the optimal design strategy in Part II [18] of our work is to use a simple parametrized family of unit cells, thus independent of the stress tensor. For that purpose, the optimal smoothing exponent $q^*(\xi, \rho, \sigma)$ has to be averaged in terms of the stress. This averaging process should not be uniform and must take into account that the resulting cells Y_0 will be used in an optimal design process. More precisely, the macroscopic structural optimization of Part II will favor some values of (ξ, ρ) for given stress σ. For example, it is well known that for compliance minimization the thickness of the "walls" of the micro-structure should be proportional to the stress that it has to sustain in its direction. This is rigorously proved for rank-2 laminates in 2-d [11] and it is a numerical evidence for rectangular holes in a square cell [29]. Note that this fact is different from the optimal orientation of orthotropic materials [19] which is already taken into account by taking $\sigma_{12} = 0$. Intuitively, the macroscopic optimization algorithm will tend to propose large/elongated rectangular holes when dealing with pure traction stresses and more symmetric holes when dealing with more hydrostatic loads.

Therefore, it is likely that micro-structures which have a semi-axis ratio m_1/m_2 will be favored by the structural optimization process at places where the stress tensor ratio $|\sigma_{11}|/|\sigma_{22}|$ has similar values. Note that the ratio σ_{11}/σ_{22} may be positive or negative, so its absolute value is close to m_1/m_2 if $\phi \sim \xi$ or $\phi \sim \pi - \xi$. In other words, the average of $q^*(\xi, \rho, \phi)$ is performed with a non-uniform weight in terms of ϕ, which is proportional to how close is the ratio of the principal stresses with the semi-axis ratio ξ and $\pi - \xi$. Then, we propose to compute the averaged optimal smoothing exponent as follows

$$q_N(\xi, \rho) = \frac{1}{2}\int_0^{2\pi} P(\phi - \xi) q^*(\xi, \rho, \varphi(\phi)) d\phi + \frac{1}{2}\int_0^{2\pi} P(\phi - (\pi - \xi)) q^*(\xi, \rho, \varphi(\phi)) d\phi \tag{38}$$

where $P(\phi)$ is the Gaussian probability function, with parameter $s > 0$ (in the sequel $s = 0.1$), defined by

$$P(\phi) = \frac{1}{\sqrt{2\pi s^2}} \exp^{-\frac{\phi^2}{2s^2}}.$$

In (38) it is implicitly assumed that the functions of ϕ are 2π-periodic. In particular, the symmetry property (36) is used to define $\varphi(\phi)$ and thus the optimal smoothing exponent is well defined for $\phi \in [0, 2\pi]$ although it has been explicitly computed only for $\varphi \in [0, \pi]$. The fast decrease of the Gaussian probability function, due to the small value of parameter s, allows us to truncate $P(\phi)$ to 0 when $|\phi| \geq \pi/8$, without any loss of accuracy. Similarly, the standard deviation of the optimal smoothing exponent is defined as

$$\begin{aligned} s_q(\xi, \rho) &= \frac{1}{2}\int_0^{2\pi} P(\phi - \xi) \left| q^*(\rho, \xi, \varphi(\phi)) - q_N(\rho, \xi) \right|^2 d\phi \\ &+ \frac{1}{2}\int_0^{2\pi} P(\phi - (\pi - \xi)) \left| q^*(\rho, \xi, \varphi(\phi)) - q_N(\rho, \xi) \right|^2 d\phi. \end{aligned} \tag{39}$$

In Figure 9, we plot in blue some optimal smoothing exponent q^* for different sample points (ξ, ρ) of the admissible design space $\mathcal{V}_{ad}^R$ and in black the mean value q_N computed according to (38). We also plot the micro-structure with the optimal super-ellipsoidal hole for different stress angles ϕ and its corresponding macroscopic stress load. In red, the Gaussian probability function centred on ξ and $\pi - \xi$ is displayed.

In the left image of Figure 9, which corresponds to a small horizontal and elongated super-ellipsoidal hole, we observe that the optimal smoothing exponent is almost constant (around a value of 15) for all stress cases, except for a strong oscillation near $\phi = \pi/2$, which corresponds to a horizontal traction stress load case. This is because, as can be seen in Figure 8b, for $\phi \sim \pi/2$ the stress norm $J_\infty(q)$ is almost flat with respect to the smoothing exponent q and consequently the mesh discretization artificially determines the optimal smoothing exponent. The weighted mean value $q_N(\xi, \rho)$ of the

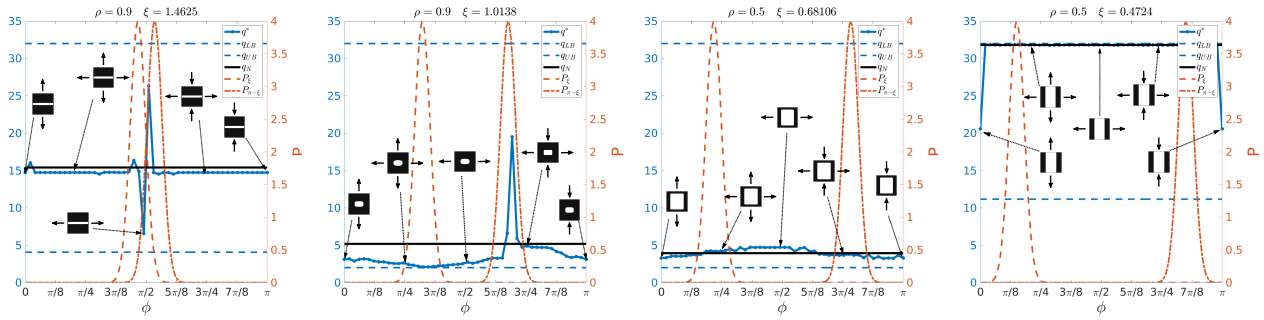

Figure 9: In blue: optimal smoothing exponent $q^*(\xi, \rho, \phi)$ for different super-ellipsoidal holes as a function of the stress angle ϕ. In red: Gaussian probability functions to average the optimal smoothing exponent according to (38). In black: averaged optimal smoothing exponent $q_N(\xi, \rho)$.

smoothing exponent, from now on called averaged smoothing exponent, is the horizontal black line, which is clearly very close to the blue curve of the optimal smoothing exponent $q^*(\xi, \rho, \phi)$.

In the second left image of Figure 9, which corresponds to a small and quite symmetric super-ellipsoidal hole, the optimal smoothing exponent is again roughly constant, except for one peak around $\phi \sim (\pi - \xi)$, and its averaged value is smaller than the previous one for the horizontal hole. Again, this is due to the flatness of the stress norm function with respect to the smoothing exponent. In this case, the standard deviation is larger.

In the third and fourth left images of Figure 9, which correspond to two large super-ellipsoidal holes, one symmetric and the other vertical, the optimal smoothing exponent is almost constant for all stress angles. Its value is small for the first case and large for the second one. Thus, in both cases, the mean value $q_N(\xi, \rho)$ is a very accurate approximation (small standard deviation). Overall, we may conclude that: (i) elongated ($|\xi - \pi/4| >> 1$) super-ellipsoidal holes entail large value of the optimal smoothing exponent q^*, while on the contrary quite symmetric ($|\xi - \pi/4| << 1$) super-ellipsoidal holes yield small values of q^*; (ii) the optimal smoothing exponent q^* depends weakly on the macroscopic stress load in the sense that it is almost constant except for one peak or oscillation; (iii) even when the standard deviation of the optimal smoothing exponent q^* is large, the stress norm of the mean value $J_\infty(q_N)$ is very similar to the stress norm of the optimal exponent $J_\infty(q^*)$ because the stress norm function $J_\infty(q)$ is very flat. Consequently, averaging (non-uniformly) the optimal smoothing exponent q^* in terms of the macroscopic stress load is a suitable and reasonable simplification.

5.3 Regularized smoothing exponent for the super-ellipsoidal hole

Behaviour of the averaged smoothing exponent. After solving the optimization problem (33), delivering the optimal smoothing exponent $q^*(\xi, \rho, \sigma)$, the weighted average, presented in (38), is applied to get the averaged smoothing exponent $q_N(\xi, \rho)$. We now investigate the behaviour of $q_N(\xi, \rho)$ with respect to its variables. The first row of Figure 10 displays the standard deviation of q_N, the averaged smoothing exponent q_N and its regularization q_A in the (ξ, ρ)-plane. Note that these three plots are symmetric with respect to the vertical line $\xi = \pi/4$ because $\tan(\pi/2 - \xi) = 1/\tan(\xi)$, which amounts to exchange m_1 and m_2, i.e. to rotate by $\pi/2$ the microstructure. The second row of Figure 10 displays the same quantities in the (m_1, m_2)-plane. Recall that (28) gives a formula for m_1 and m_2 in terms of (q_N, ξ, ρ). In Figure 10b is plotted the averaged smoothing exponent $q_N(\xi, \rho)$. We first observe that for extreme values of the semi-axis, $\xi \to \xi_{LB}(\rho)$ or $\xi \to \xi_{UB}(\rho)$ (see their precise definitions in (5.3) below), namely for very elongated holes, the value of q_N is very large and thus the averaged super-ellipsoidal holes are rectangular holes (with slightly rounded corners). The dependency of q_N with the size of the hole for quite symmetric holes (ξ close to $\pi/4$) features three different regimes. When the hole is very large (small ρ), rectangular holes with rounded corners are preferred (large q_N). For intermediate size holes ($\rho \sim [0.2, 0.9]$), rounded holes (small q_N) are preferred. For very small holes (large ρ), although some oscillations appear, rectangular holes with rounded corners (large q_N) seems to be preferred. In Figure 10a the standard deviation $s_q(\xi, \rho)$ is displayed, allowing to quantify the averaging of the optimal smoothing exponent q^*. Clearly, the averaged value q_N is a significantly

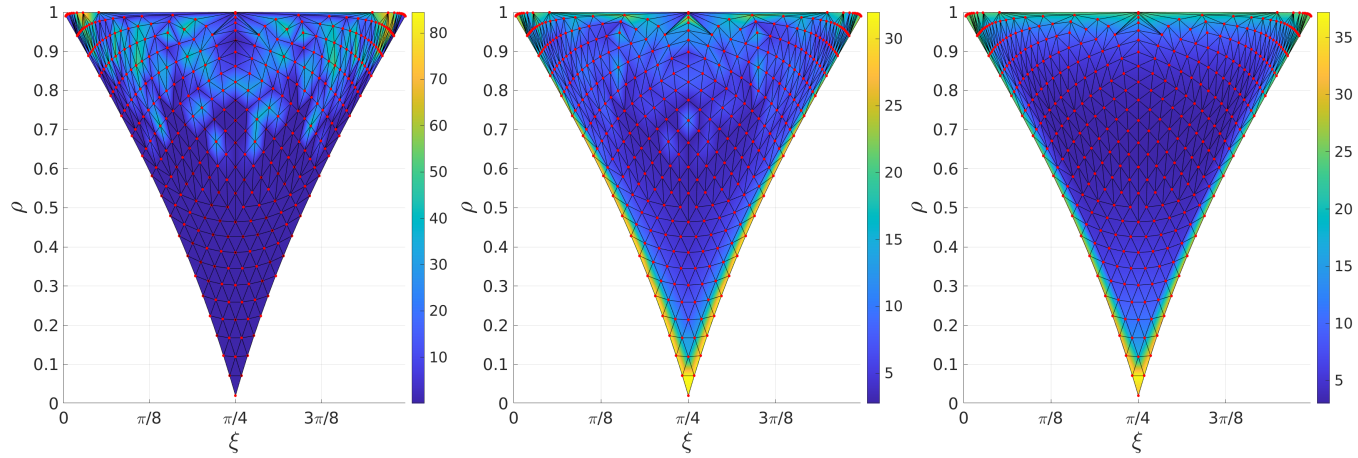

(a) Standard deviation $s_q(\xi, \rho)$ of the optimal smoothing exponent

(b) Averaged smoothing exponent $q_N(\xi, \rho)$

(c) Regularized optimal smoothing exponent $q_A(\xi, \rho)$

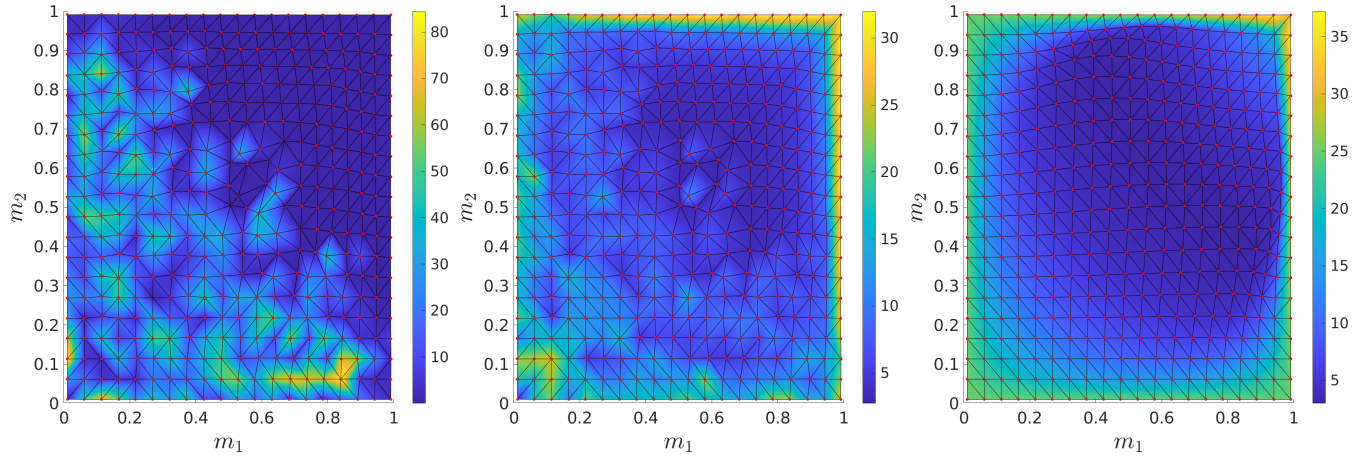

(d) Standard deviation $s_q(m_1, m_2)$ of the optimal smoothing exponent

(e) Averaged smoothing exponent $q_N(m_1, m_2)$

(f) Regularized optimal smoothing exponent $q_A(m_1, m_2)$

Figure 10: Averaged smoothing exponent and its regularization.

accurate representation of the optimal smoothing exponent q^* for a large range of super-ellipsoidal sizes ($\rho \in [\rho_{min}, 0.7]$). For small super-ellipsoidal holes ($\rho \in [0.7, 1]$), especially when they are elongated ($\xi \to \xi_{LB}$ or $\xi \to \xi_{UB}$), the optimal smoothing exponent significantly varies when considering different stress load cases. However, the experiments showed us that these oscillations have a limited impact since the stress norm function $J_\infty(q)$ is flat in these situations.

Regularization by an analytical expression. To simplify and regularize the behaviour of the averaged smoothing exponent $q_N(\xi, \rho)$ (shown in Figure 10b), we propose an analytic expression to approximate and regularize q_N. There are many possible ways for regularizing q_N but, after some trial and error, we choose the following procedure. First, recall that, for given ρ, the semi-axis ratio ξ varies in the range $(\xi_{LB}(\rho); \xi_{UB}(\rho))$, which is defined by

$$\xi_{LB}(\rho) = \max\Big(\xi_1(m_{L_1}, q_{\min}, \rho), \xi_2(m_{U_2}, q_{\max}, \rho)\Big)$$
$$\xi_{UB}(\rho) = \min\Big(\xi_1(m_{U_1}, q_{\max}, \rho), \xi_2(m_{L_2}, q_{\min}, \rho)\Big).$$

where the functions ξ_1 and ξ_2 are already introduced in (29). Since $q_N(\xi, \rho)$ is symmetric with respect to the vertical line $\xi = \pi/4$, its regularization $q_A(\xi, \rho)$ is built to have the same symmetry. It is defined as a combination of two approximations, $q_{\xi_{\pi/4}}(\rho)$ which approximates $q_N(\pi/4, \rho)$, and $q_{\xi_{UB}}(\rho)$ which

approximates $q_N(\xi_{UB}(\rho),\rho)$ (and by symmetry also $q_N(\xi_{LB}(\rho),\rho)$), namely

$$q_A(\xi,\rho) = (1-\xi_A(\xi,\rho)^\alpha)\, q_{\xi_{\pi/4}}(\rho) + \xi_A(\xi,\rho)^\alpha q_{\xi_{UB}}(\rho)$$

where $\alpha > 0$ is a parameter to be chosen and $0 \le \xi_A(\xi,\rho) \le 1$ is defined as a rescaled version of ξ by

$$\xi_A(\xi,\rho) = \frac{|\xi - \pi/4|}{\xi_{UB}(\rho) - \pi/4}.$$

The upper bound approximation $q_{\xi_{UB}}(\rho)$ is defined as a combination of the values of the averaged smoothing exponent in ρ_{min} and ρ_{max}. Denoting $q_{\rho_{min}} = q_N(\xi_{UB}(\rho_{min}),\rho_{min})$ and $q_{\rho_{max}} = q_N(\xi_{UB}(\rho_{max}),\rho_{max})$, we introduce

$$q_{\xi_{UB}}(\rho) = \left(1-\rho_A(\rho)^\beta\right) q_{\rho_{min}} + \rho_A(\rho)^\beta q_{\rho_{\max}}$$

where $\beta > 0$ is a parameter to be chosen and $0 \le \rho_A(\rho) \le 1$ is defined as

$$\rho_A(\rho) = \frac{\rho - \rho_{\min}}{\rho_{\max} - \rho_{\min}} \quad \text{with} \quad \rho_{\min} = 0.0199, \quad \rho_{\max} = 0.9999.$$

The approximation $q_{\xi_{\pi/4}}(\rho)$ for $\xi = \pi/4$ is defined by

$$q_{\xi_{\pi/4}}(\rho) = \frac{A\rho^2 + B\rho + C}{D\rho^2 + E\rho + 1},$$

where the constants A, B, C, D and E are determined by imposing the equality $q_{\xi_{\pi/4}}(\rho) = q_N(\pi/4,\rho)$ at $\rho_{\min} = 0.0199$, $\rho_{\max} = 0.9999$, $\rho_s = 0.2$ and at the minimum point ρ_m of $q_{\xi_{\pi/4}}(\rho)$. In view of the values of $q_N(\xi,\rho)$ in Figure 10b, we impose that $q_{\xi_{\pi/4}}(\rho_{\min}) = 32$, $q_{\xi_{\pi/4}}(\rho_{\max}) = 25$, $q_{\xi_{\pi/4}}(\rho_m) = 3$. The other parameters, $\alpha = 20.252$, $\beta = 0.543$, $\rho_m = 0.649$ and $q_{\rho_s} := q_{\xi_{\pi/4}}(\rho) = 11.779$, are obtained by solving the least square problem

$$\min_{\alpha,\beta,\rho_m,q_{\rho_s}} e_r = \frac{||q_N - q_A(\alpha,\beta,\rho_m,q_{\rho_s})||^2}{||q_N||^2} \quad \text{with} \quad ||q||^2 = \int_{\rho_{\min}}^{\rho_{\max}} \int_{\xi_{LB}(\rho)}^{\xi_{UB}(\rho)} q(\xi,\rho)^2 d\xi d\rho$$

The relative error at the solution is $e_r = 0.082$. The optimal values of the constants are $A \approx 52.8$, $B \approx -82.0$, $C \approx 37.4$, $D \approx -6.8$, $E = 6.2$. The regularized smoothing exponent q_A in terms of (ξ,ρ) and (m_1,m_2) is depicted in Figures 10c and 10f: it is quite close to the averaged smoothing exponent q_N (which is computed numerically) but with less oscillations, as could be expected. Figure 11 displays a cross section, along the vertical line $\xi = \pi/4$, of the two exponents q_A and q_N, as functions of ρ. From now on, we use the analytical smoothing exponent q_A, instead of q_N, for computing the optimal

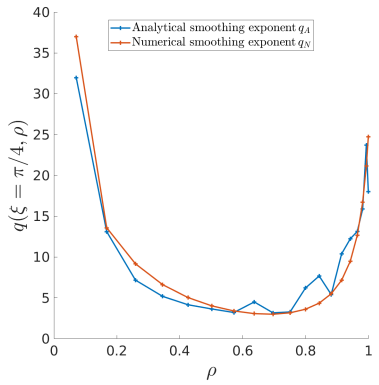

Figure 11: Analytical smoothing exponent $q_A(\xi = \pi/4,\rho)$ and averaged smoothing exponent $q_N(\xi = \pi/4,\rho)$.

super-ellipsoidal holes.

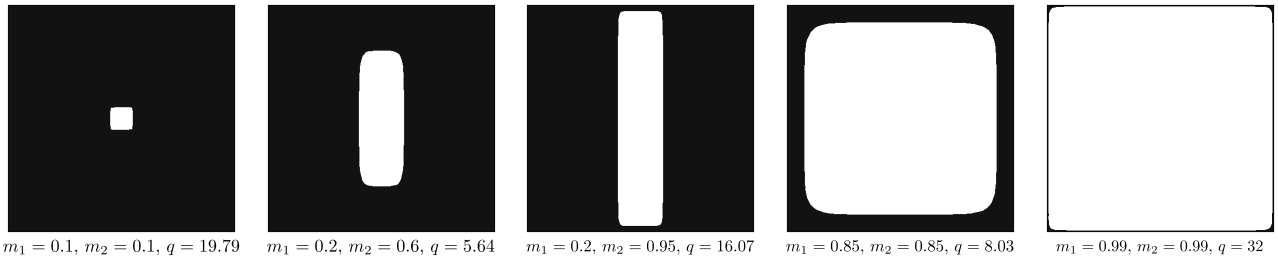

Figure 12: Some optimal super-ellipsoidal holes that minimize the maximum stress norm J_∞.

Some optimal micro-structures. For a more visual description of the proposed optimal micro-structures, we plot in Figure 12 some of them. As observed in the numerical experiments, they range from circular and ellipsoidal holes (for small holes) to some limit cases (large square, elongated rectangular holes).

5.4 Homogenized and amplification tensors for optimal super-ellipsoidal holes

Once optimal super-ellipsoidal holes have been obtained by the process just described and based on maximal stress minimization, it is time to exhibit their homogenized properties.

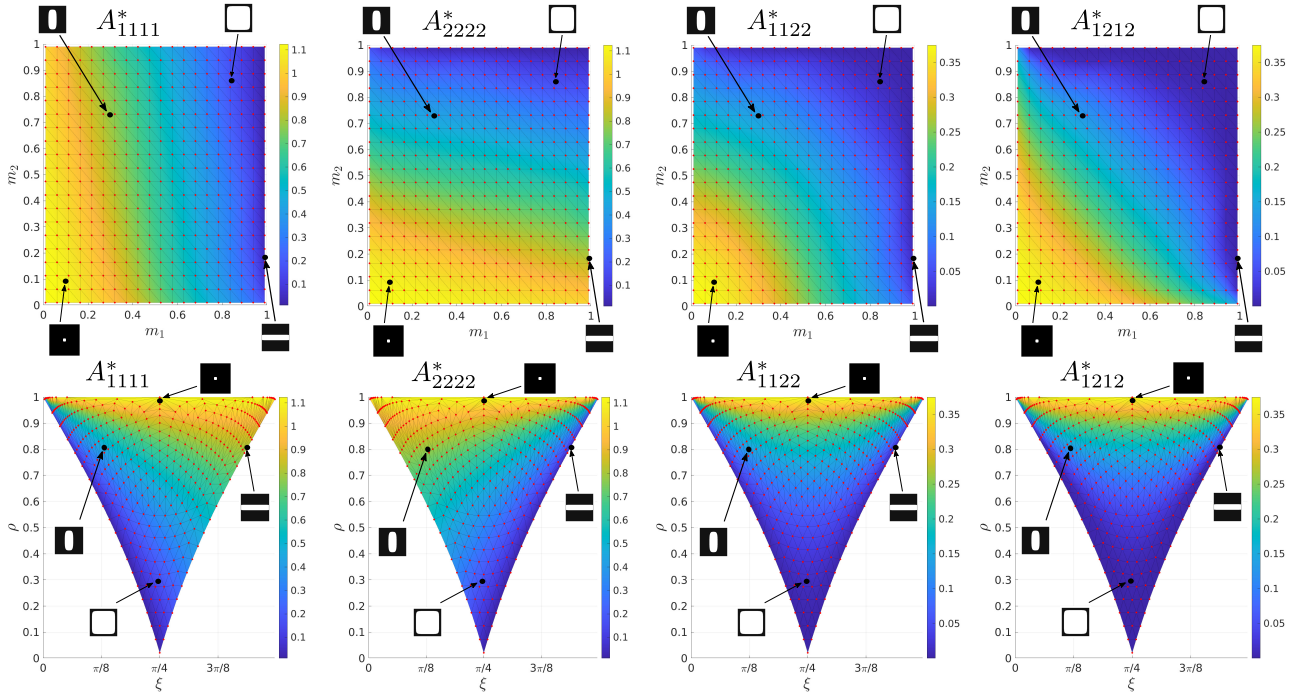

Figure 13: Entries of the homogenized tensor A^* for the super-ellipsoidal hole with smoothing exponent $q_A(\xi, \rho)$.

Homogenized tensor A^*. In Figure 13, the entries of the homogenized tensor are plotted for the super-ellipsoidal hole with smoothing exponent $q_A(\xi, \rho)$. Note that for the exponent q_A, the range of the admissible values of parameters (ξ, ρ) is identical to the admissible design space for rectangular holes $\mathcal{V}^R_{ad}$. This means that when solving the macroscopic stress minimization problem, detailed in Part II [18], (almost) void micro-structure could be considered. Due to horizontal and vertical symmetry, the entries A^*_{1112} and A^*_{2212} are zero and therefore are not displayed in Figure 13. The entries A^*_{1111} and A^*_{2222} strongly (and monotonically) depends on m_1 and m_2 respectively. Instead, the entries A^*_{1122} and A^*_{1212} strongly (and monotonically) depends on the volume fraction ρ. Again for a fix volume fraction ρ, elongated horizontal holes ($m_1 \to 1$), this is of the rank-1 nature, exhibit large values of the entry A^*_{1111}. The same for A^*_{2222} with vertical elongated holes.

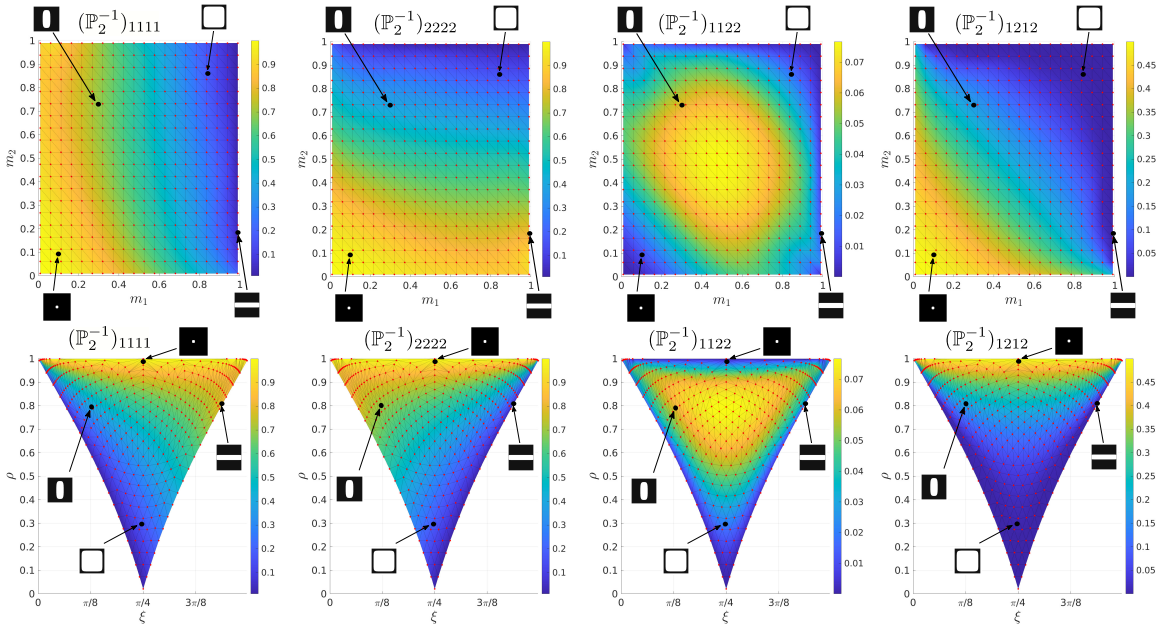

Figure 14: Inverse of the amplification tensor for the super-ellipsoidal hole with smoothing exponent $q_A(\xi, \rho)$.

Amplification tensor with $p = 2$. In Figure 14 is plotted the inverse of the amplification tensor (in the case $p = 2$) for the super-ellipsoidal hole with smoothing exponent $q_A(\xi, \rho)$. We observe the strong dependency of $(\mathbb{P}_2^{-1})_{1111}$ with respect to m_1 and that of $(\mathbb{P}_2^{-1})_{2222}$ with m_2. The entry $(\mathbb{P}_2^{-1})_{1122}$ has a maximum in $\xi = \pi/4$ (symmetric hole) and $\rho = 0.8$, while $(\mathbb{P}_2^{-1})_{1212}$ is monotonically increasing with the volume fraction ρ.

5.5 Comparing optimal super-ellipsoidal holes with rectangular holes

To quantify the gain obtained by the optimization process, we compare the optimal super-ellipsoidal hole (featuring the smoothing exponent $q_A(\xi, \rho)$) with a rectangular hole in terms of rigidity and stress norm.

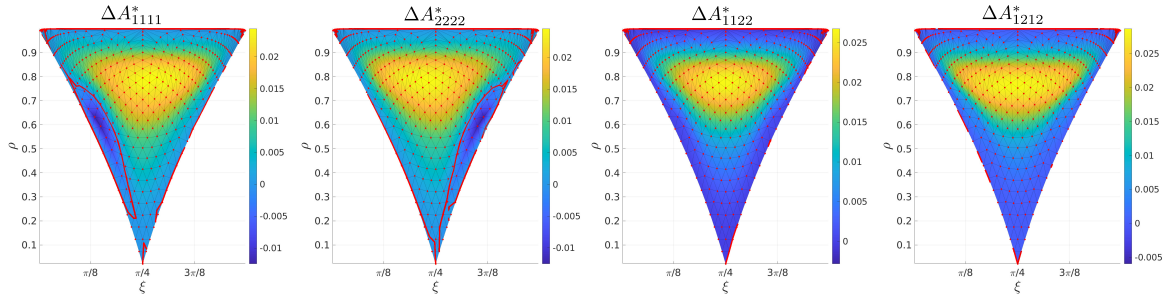

Figure 15: Difference of the homogenized tensors between the optimal super-ellipsoidal and rectangular holes.

Homogenized tensor A^*. In Figure 15, we plot the difference, denoted by ΔA^*, of the homogenized tensors between the micro-structures with an optimal super-ellipsoidal hole and a rectangular hole. Where ΔA^* is positive, optimal super-ellipsoidal holes outperforms rectangular holes in terms of rigidity and vice-versa. The zero level-set line, $\Delta A^* = 0$, is depicted in red to clearly distinguish both positive and negative regions. We observe that in almost all situations, the optimal super-ellipsoidal hole outperforms, in terms of rigidity, the rectangular hole. The maximum gain in terms of rigidity occurs for symmetric holes $\xi = \pi/4$ ($m_1 = m_2$) and volume fractions around $\rho = 0.8$. We recall that the limits $\xi \to \xi_{UB}$ and $\xi \to \xi_{LB}$ corresponds to the limit cases $m_1 \to 1$ and $m_2 \to 1$, namely very elongated holes in the horizontal or vertical direction, respectively. Those very elongated holes behave like rank-1

laminates. Note that in the elongated horizontal limit case $\xi \to \xi_{UB}$ (or $m_1 \to 1$), the optimal super-ellipsoidal hole behaves as the rectangular hole in terms of stiffness in the horizontal direction: see ΔA^*_{1111} when $\xi \to \xi_{UB}$. Of course, a symmetric situation occurs for vertically elongated holes ($\xi \to \xi_{LB}$ or $m_2 \to 1$) when looking at ΔA^*_{2222}.

Amplification tensor. In Figure 16, we plot the difference, denoted by $\Delta\mathbb{P}_2^{-1}$, of the inverse amplification tensors between the micro-structures with an optimal super-ellipsoidal hole and a rectangular hole. Where $\Delta\mathbb{P}_2^{-1}$ is positive, optimal super-ellipsoidal holes outperforms rectangular holes since they have a lower stress amplification tensor and vice-versa. Clearly, the gain is more marked for the entries $(\mathbb{P}_2^{-1})_{1111}$ and $(\mathbb{P}_2^{-1})_{2222}$ than for $(\mathbb{P}_2^{-1})_{1122}$ and $(\mathbb{P}_2^{-1})_{1212}$ where the differences are of the order of 10^{-3}. According to Figure 16, the super-ellipsoidal hole outperforms the rectangular hole in most cases. However, there is a small zone where the rectangular hole outperforms the super-ellipsoidal hole. To understand this result, we analyse in more detail the difference of the $(\mathbb{P}_2^{-1})_{1111}$ entry (symmetric analysis for $(\mathbb{P}_2^{-1})_{2222}$) in the following four cases:

- **Medium size symmetric holes** ($\rho \in [0.2, 0.8]$, $\xi \sim \pi/4$): in this case the optimal super-ellipsoidal hole is clearly better than the rectangular hole because it amplifies less the stress $\sigma^{\text{loc}}_{11}(y)$ when loading with an uni-axial horizontal macroscopic stress tensor $\sigma = [1\ 0\ 0]$. This is because, the high stress are caused here only by the corners of the hole, which for the optimal smoothing exponent case have been optimally rounded.

- **Small and large size holes** ($\rho \in [0.8, \rho_{\max}]$ and $\rho \in [\rho_{\min}, 0.2]$): the behaviours of the optimal super-ellipsoidal hole and of the rectangular hole are very similar.

- **Medium size horizontally elongated holes** ($\rho \in [0.2, 0.8]$, $\xi \to \xi_{UB}$)**:** again for this type of microstructure, which is like a rank-1 laminate, the behaviours of the optimal super-ellipsoidal hole and of the rectangular hole are very similar.

- **Medium size vertically elongated holes** ($\rho \in [0.2, 0.8]$, $\xi \to \xi_{LB}$)**:** we observe that the rectangular hole amplifies less the stress norm (with $p = 2$). The reason for this lower performance of the optimal super-ellipsoidal hole is clear. In such a case, high stresses have two distinct origins: they are created by the corners of the hole but also by the thin horizontal ligaments which separate the hole from the top and bottom boundary of the cell. See third image of Figure 12. Optimal super-ellipsoidal holes smooth the corners at the cost of reducing the thickness of these thin bars. Since the high stresses occupy a larger zone in these thin bars than around the corners, and because these stresses are averaged by the $p = 2$ norm to obtain the value of $\mathbb{P}_2$, it turns out that rectangular holes have a smaller stress norm despite their square corners. If we had compared the stress amplification tensor $\mathbb{P}_p$ for a much larger exponent $p > 2$, the optimal super-ellipsoidal hole would have superseded the rectangular hole. Eventually, it is worth noticing that, in the further process of macroscopic optimization (using the methodology proposed in [1]), the present case of a very elongated vertical hole loaded with an uni-axial horizontal macroscopic stress is very unlikely to be optimal and should not appear in practice.

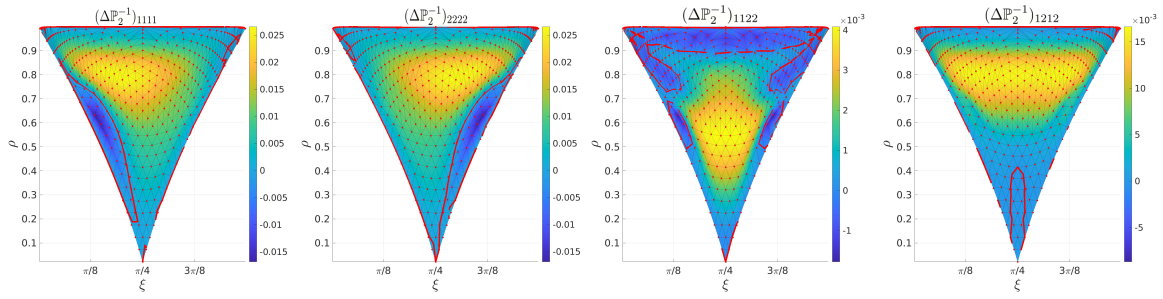

Figure 16: Difference of the inverse amplification tensors between the optimal super-ellipsoidal and rectangular holes.

6 Relation with the Vigdergauz micro-structure

For minimizing the stress concentration, we proposed a super-ellipsoidal hole with an optimal smoothing exponent. There is another well-known periodic micro-structure which is known to be optimal for stress distribution which is the so-called Vigdergauz micro-structure [22]. More precisely, for a macroscopic stress tensor with same sign principal stresses, the Vigdergauz micro-structure is the most rigid one for compliance minimization and is also minimizing the maximal stress norm in the cell [23]. In particular, the boundary of the hole is equi-stressed and [23] proposed an implicit expression of the boundary of the Vigdergauz micro-structure in terms of the macroscopic strains (or macroscopic stress) and the volume fraction (apart from the material properties). More recently, Liu et al. proposed in work [30] an alternative expression in terms of the volume fraction and another (non-intuitive) geometrical variable. The goal of this section is to numerically compare our micro-structure featuring a super-ellipsoidal hole with the Vigdergauz micro-structure. The conclusion is that they are very similar and the differences between their shapes is negligible in practice.

Therefore, we favor super-ellipsoidal holes because the Vigdergauz micro-structures have a very complex parametrization which is not easy to handle numerically. In fact, it is not explicit and depends on elliptic integrals and requires finding zeros of non-linear equations. This makes the super-ellipsoidal hole more convenient in terms of simplicity and computational cost.

Level-set description of Vigdergauz micro-structure. Let us first provide a description of the Vigdergauz micro-structure through the zero value of a level-set function. Early work [23] described the Vigdergauz micro-structure in terms of the macroscopic strain and volume fraction (and material) parameters. In [30], the Vigdergauz micro-structure is described by a symmetry (non-intuitive) parameter r and the volume fraction ρ. Here, we slightly modify the parametrization of the last work by using the semi-axis ratio ξ instead and the volume fraction parameter ρ, as we did for computing the optimal super-ellipsoidal hole. In both works [23] and [30], a parametric description of the curve is provided. However, this is not enough for representing the micro-structure in terms of the zero value of a level-set function which is in general more appropriate in a topology optimization framework. In this work, we provide such implicit description of the micro-structure and its corresponding level-set. In the unit square cell Y with coordinates (y_1, y_2), the level-set function of the Vigdergauz micro-structure is defined as

$$\psi_v(y_1, y_2) = \begin{cases} \psi_0 & |y_1| \leq \frac{m_1}{2} \quad \text{and} \quad |y_2| \leq \frac{m_2}{2} \\ c_0 & \text{otherwise} \end{cases} \tag{40}$$

with the function $\psi_0(y_1, y_2)$ defined by

$$\psi_0(y_1, y_2) = (1 - y_{p_1}^2)(1 - y_{p_2}^2) - R.$$

The fact that ψ_v is not continuous at the boundary of the inner rectangle $(-m_1/2, m_1/2)\times(-m_2/2, m_2/2)$ does not matter here since only its sign is important. Thus, the value of $c_0 < 0$ can be taken arbitrarily but negative. In this work, we take $c_0 = -|\psi_0|$. The coordinates y_{p_1} and y_{p_2} are computed as

$$y_{p_1} = F^{-1}(\frac{y_1 f_1}{m_1/2}, r_1) \quad \text{and} \quad y_{p_2} = F^{-1}(\frac{y_2 f_2}{m_2/2}, r_2)$$

and the parameters $f_1 = F(\sqrt{1-R}, r_1)$ and $f_2 = F(\sqrt{1-R}, r_2)$, where $R = (1 - r_1)(1 - r_2)/(r_1 r_2)$. The function $F(t, k)$ is the incomplete elliptic integral of first kind defined by

$$F(t, k) = \int_0^t \frac{dx}{\sqrt{(1 - x^2)\,(1 - kx^2)}}.$$

and $F^{-1}(t, k)$ is the Jacobi elliptic function, precisely defined as the inverse of $t \to F(t, k)$. Both functions are implemented in almost all numerical software packages. The semi-axis parameters m_1 and m_2 of the Vigdergauz micro-structures can be expressed only in terms of r_1 and r_2 as

$$m_1 = \frac{1 - t_2}{1 - t_1 t_2} s_1 \quad \text{and} \quad m_2 = \frac{1 - t_1}{1 - t_1 t_2} s_2$$

where the parameters t_1, t_2, s_1 and s_2 are given by

$$t_1 = \frac{F(1, 1-r_1)}{F(1, r_1)}, \qquad s_1 = \frac{f_1}{F(1, r_1)},$$
$$t_2 = \frac{F(1, 1-r_2)}{F(1, r_2)}, \qquad s_2 = \frac{f_2}{F(1, r_2)}.$$

Knowing the values of the parameters r_1 and r_2, we can explicitly compute the level-set function (40). Such values are determined by imposing a priori given values for the semi-axis ratio ξ and volume fraction ρ. This is done by solving the following two non-linear equations

$$\tan(\xi) = \frac{m_1}{m_2} = \frac{1-t_2}{1-t_1}\frac{s_1}{s_2} \tag{41}$$
$$\rho = 1 - \frac{t_1(1-t_2) + t_2(1-t_1)}{(1-t_1 t_2)}. \tag{42}$$

with r_1 and r_2 as unknowns, which are bounded by $0 < r_1 < 1$ and $0 < r_2 < 1$. Note that all variables that appear in (42) depend only on r_1 and r_2. In this work, we used two nested bisection loops to

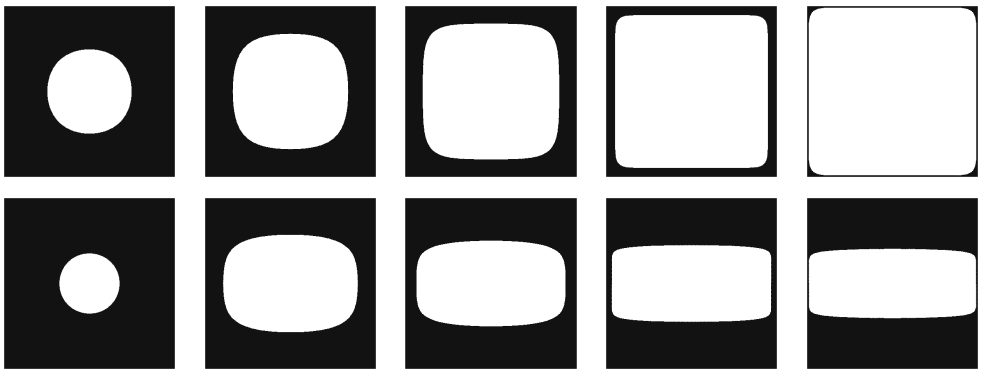

Figure 17: Vigdergauz micro-structures examples

solve these two non-linear equations. In Figure 17, some examples of the Vigdergauz micro-structures are plotted which look reasonably similar to square micro-structures with a super-ellipsoidal hole.

Closest super-ellipsoidal hole. From the previous analysis the level-set function of the Vigdergauz micro-structure $\psi_v(\xi, \rho)$, defined by (40), is precisely parametrized by the semi-axis ratio ξ and the volume fraction ρ. Recall that the level-set function of the super-ellipse $\psi_s(q, \xi, \rho)$, defined in (25), was characterized in terms of the volume fraction ρ, the semi-axis ratio ξ and the smoothing parameter q through equation 28. Thus, our goal is to find the best q such that both micro-structures are as close as possible in the following sense. The difference between two characteristic functions is measured with the L^1 norm which represents the volume of the difference set. For numerical reasons we rely on a smoothed version of the characteristic function which is defined by the zero level-set. We use a standard discrete (with compact support) kernel filter for the smoothing, which was introduced in [31] and is denoted by $P_1 : L^\infty(Y, \{0, 1\}) \to L^\infty(Y, [0, 1])$ where Y is the micro-structure cell domain. Thus, the optimization problem to solve is

$$\min_{q \in [q_{\min}, q_{\max}]} \int_Y |\rho_s(\xi, \rho, q) - \rho_v(\xi, \rho)| \tag{43}$$

where the densities functions $\rho_s(\xi, \rho, q)$ and $\rho_v(\xi, \rho)$ are defined as

$$\rho_s(\xi, \rho, q) = P_1(\chi_s(\xi, \rho, q)), \qquad \rho_v(\xi, \rho) = P_1(\chi_v(\xi, \rho)).$$

Thus, they are the smoothed versions of the characteristic functions

$$\chi_s(\xi, \rho, q) = \begin{cases} 0 & \psi_s(\xi, \rho, q) > 0 \\ 1 & \psi_s(\xi, \rho, q) \leq 0 \end{cases} \quad \text{and} \quad \chi_v(\xi, \rho) = \begin{cases} 0 & \psi_v(\xi, \rho) > 0 \\ 1 & \psi_v(\xi, \rho) \leq 0. \end{cases}$$

Since problem (43) is a minimization problem with respect the sole variable q, we use again a successive parabolic interpolation algorithm combined with a golden section search [28]. In Figure 18, some

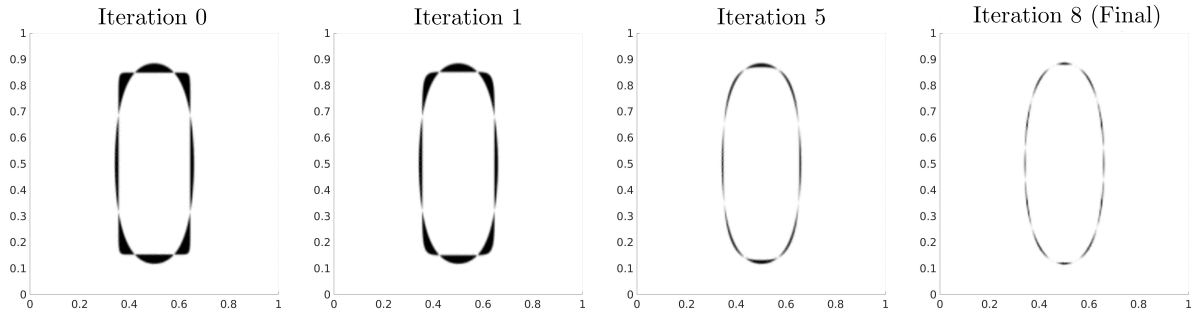

a) err $= 3.04 * 10^{-2}$, $q = 20$ b) err $= 2.68 * 10^{-2}$, $q = 9.082$ c) err $= 5.8 * 10^{-3}$, $q = 3.033$ d) err $= 4.41 * 10^{-5}$, $q = 2.316$

Figure 18: Symmetric difference between a Vigdergauz micro-structures and a square micro-structure with a super-ellipsoidal hole (from left to right, improving value of the exponent q, from 20 to 2.316). The relative error of the densities is given as err $= \frac{\int_Y |\rho_s - \rho_v|}{\int_Y |\rho_v|}$.

intermediate and the final iterations of the optimization problem (with $q_{\min} = 2$ and $q_{\max} = 32$) are shown for the hole $\xi = \pi/8$ ($m_2 = 2.41 m_1$) and $\rho = 0.8$. A triangular mesh with 102400 P1 finite elements with a total of 51521 nodes is used. Clearly, one can observe in Figure 18 that the Vigdergauz micro-structure is approximated by a super-ellipsoidal hole with a very high accuracy (negligible error). This experiment justifies the use of a super-ellipsoidal hole instead of the Vigdergauz micro-structure when minimizing the maximum stress since we can obtain similar results but with much more simplicity.

7 Conclusion

This is the first part of a work devoted to the optimization of lattice structures for stress minimization. This first part focused on the design of a family of 2-d parametrized periodicity cell which are nearly optimal for local stress minimization. These parametrized cells will be used in the second part [18] for optimizing the macroscopic lattice structures, by using a de-homogenization technique, as presented in [1] for compliance minimization.

We proposed in this work to optimize a square cell with a super-ellipsoidal hole. On the one hand, it is rich enough to generalize the standard rectangular and ellipsoidal holes and on the other hand it is simple enough to be explicitly described and further used in the de-homogenization method of Part II [18].

Before optimizing the micro-structure, two numerical experiments were performed to gain insight in the design process. First, we compared rectangular and ellipsoidal holes in terms of effective properties, as well as amplification tensors, which take into account the local increase of the stress, compared to the macroscopic stress, due to the micro-structure. Second, the amplification factors were computed for various values of the exponent p when the stress is evaluated with an L^p norm. They confirm that neither rectangles, nor ellipses are always optimal and that super-ellipses are a good compromise.

Our main result is the optimization of the exponent q, defining the super-ellipse for minimizing the maximum local stress when solving a periodic cell problem, loaded by a given macroscopic stress. For each stress load (aligned with the hole), each volume fraction and each semi-axis ratio, an optimal super-ellipse exponent q has been found. Since the goal is to design a micro-structure which depends only on geometric parameters and not on the applied stress, these optimal super-ellipse exponents were averaged with respect to the applied stress with a bias towards stresses which are more likely to appear in the macroscopic optimization of Part II. Then, for simplicity and further use, we proposed an analytical formula for approximating the optimal averaged exponent in terms of the geometrical parameters of the super-ellipsoidal hole. We observed a clear reduction of the stress norm (through the amplificator tensor) of the proposed optimal super-ellipsoidal hole with respect of the rectangular hole. As a final check of our results, we compared the optimal super-ellipsoidal hole with the Vigdergauz

micro-structure, which is known to be optimal for minimizing the maximum stress in some cases, but is not simple enough for a systematic use in numerical computations. We numerically checked that the Vigdergauz micro-structure can be approximated by an optimal super-ellipsoidal hole with high accuracy.

Acknowledgements. This work is partially supported by the SOFIA project, funded by Bpifrance (Banque Publique d'Investissement). This work has received funding from the European Union's Horizon 2020 research and innovation programme under the Marie Skłodowska-Curie grant agreement No 833092.

References

[1] Grégoire Allaire, Perle Geoffroy-Donders, and Olivier Pantz. Topology optimization of modulated and oriented periodic microstructures by the homogenization method. *Computers & Mathematics with Applications*, 78(7):2197–2229, 2019.

[2] Jeroen Groen and Ole Sigmund. Homogenization-based topology optimization for high-resolution manufacturable microstructures. *Internat. J. Numer. Methods Engrg.*, 113(8):1148–1163, 2018.

[3] Olivier Pantz and Karim Trabelsi. A post-treatment of the homogenization method for shape optimization. *SIAM J. Control Optim.*, 47(3):1380–1398, 2008.

[4] Pierre Duysinx and Martin P Bendsøe. Topology optimization of continuum structures with local stress constraints. *International journal for numerical methods in engineering*, 43(8):1453–1478, 1998.

[5] Pierre Duysinx and Ole Sigmund. New developments in handling stress constraints in optimal material distribution. In *7th AIAA/USAF/NASA/ISSMO symposium on multidisciplinary analysis and optimization*, page 4906, 1998.

[6] Chau Le, Julian Norato, Tyler Bruns, Christopher Ha, and Daniel Tortorelli. Stress-based topology optimization for continua. *Structural and Multidisciplinary Optimization*, 41(4):605–620, 2010.

[7] Daniel M De Leon, Joe Alexandersen, Jun SO Fonseca, and Ole Sigmund. Stress-constrained topology optimization for compliant mechanism design. *Structural and Multidisciplinary Optimization*, 52(5):929–943, 2015.

[8] Grégoire Allaire and François Jouve. Minimum stress optimal design with the level set method. *Engineering analysis with boundary elements*, 32(11):909–918, 2008.

[9] Samuel Amstutz and Antonio A Novotny. Topological optimization of structures subject to von mises stress constraints. *Structural and Multidisciplinary Optimization*, 41(3):407–420, 2010.

[10] Renato Picelli, Scott Townsend, Christopher Brampton, Julian Norato, and H Alicia Kim. Stress-based shape and topology optimization with the level set method. *Computer methods in applied mechanics and engineering*, 329:1–23, 2018.

[11] Grégoire Allaire. *Shape optimization by the homogenization method*, volume 146. Springer Science & Business Media, 2012.

[12] Robert Lipton. Design of functionally graded composite structures in the presence of stress constraints. *International journal of solids and structures*, 39(9):2575–2586, 2002.

[13] Robert Lipton and Michael Stuebner. Optimization of composite structures subject to local stress constraints. *Computer methods in applied mechanics and engineering*, 196(1-3):66–75, 2006.

[14] Grégoire Allaire, François Jouve, and Hervé Maillot. Topology optimization for minimum stress design with the homogenization method. *Structural and Multidisciplinary Optimization*, 28(2-3):87–98, 2004.

[15] Damiano Pasini, Ahmed Moussa, and Amirmohammad Rahimizadeh. Stress-constrained topology optimization for lattice materials. *Encyclopedia of Continuum Mechanics*, pages 1–19, 2018.

[16] Lin Cheng, Jiaxi Bai, and Albert C. To. Functionally graded lattice structure topology optimization for the design of additive manufactured components with stress constraints. *Computer Methods in Applied Mechanics and Engineering*, 344:334 – 359, 2019.

[17] Perle Geoffroy-Donders. *Homogenization method for topology optimization of structures built with lattice materials.* Phd thesis, Ecole Polytechnique, December 2018. https://hal.archives-ouvertes.fr/tel-02000854.

[18] Alex Ferrer, Perle Geoffroy-Donders, and Grégoire Allaire. Stress minimization for lattice structures. Part II: Macroscopic optimization. *Manuscript in preparation*, 2020.

[19] Pauli Pedersen. On optimal orientation of orthotropic materials. *Structural Optimization*, 1(2):101–106, 1989.

[20] Lise Noël and Pierre Duysinx. Shape optimization of microstructural designs subject to local stress constraints within an xfem-level set framework. *Structural and Multidisciplinary Optimization*, 55(6):2323–2338, 2017.

[21] Pedro G Coelho, José M Guedes, and João B Cardoso. Topology optimization of cellular materials with periodic microstructure under stress constraints. *Structural and Multidisciplinary Optimization*, 59(2):633–645, 2019.

[22] Shmuel Vigdergauz. Two-Dimensional Grained Composites of Extreme Rigidity. *Journal of Applied Mechanics*, 61(2):390–394, 06 1994.

[23] Yury Grabovsky and Robert V Kohn. Microstructures minimizing the energy of a two phase elastic composite in two space dimensions. i: the confocal ellipse construction. *Journal of the Mechanics and Physics of Solids*, 43(6):933–947, 1995.

[24] Grégoire Allaire and Micol Amar. Boundary layer tails in periodic homogenization. *ESAIM Control Optim. Calc. Var.*, 4:209–243, 1999.

[25] Yury Grabovsky and Robert V Kohn. Microstructures minimizing the energy of a two phase elastic composite in two space dimensions. ii: the vigdergauz microstructure. *Journal of the Mechanics and Physics of Solids*, 43(6):949–972, 1995.

[26] Charles Dapogny, Cécile Dobrzynski, and Pascal Frey. Three-dimensional adaptive domain remeshing, implicit domain meshing, and applications to free and moving boundary problems. *Journal of computational physics*, 262:358–378, 2014.

[27] Alex Ferrer, Perle Geoffroy-Donders, and Grégoire Allaire. Supplementary material for: *Stress minimization for lattice structures. Part I: Micro-structure design.* 2020.

[28] George Elmer Forsythe, Michael A Malcolm, and Cleve B Moler. *Computer methods for mathematical computations*, volume 259. Prentice-Hall Englewood Cliffs, NJ, 1977.

[29] Martin Philip Bendsøe and Noboru Kikuchi. Generating optimal topologies in structural design using a homogenization method. *Comput. Methods Appl. Mech. Engrg.*, 71(2):197–224, 1988.

[30] Liping Liu, Richard D James, and Perry H Leo. Periodic inclusion—matrix microstructures with constant field inclusions. *Metallurgical and Materials Transactions A*, 38(4):781–787, 2007.

[31] Samuel Amstutz, Charles Dapogny, and Àlex Ferrer. A consistent relaxation of optimal design problems for coupling shape and topological derivatives. *Numerische Mathematik*, 140(1):35–94, 2018.